National Library of Canada

Acquisitions and Bibliographic Services Branch

395 Wellington Street
Ottawa, Ontario
K1A 0N4

Bibliothèque nationale du Canada

Direction des acquisitions et des services bibliographiques

395, rue Wellington
Ottawa (Ontario)
K1A 0N4

Your file Votre référence

Our file Notre référence

NOTICE

The quality of this microform is heavily dependent upon the quality of the original thesis submitted for microfilming. Every effort has been made to ensure the highest quality of reproduction possible.

If pages are missing, contact the university which granted the degree.

Some pages may have indistinct print especially if the original pages were typed with a poor typewriter ribbon or if the university sent us an inferior photocopy.

Reproduction in full or in part of this microform is governed by the Canadian Copyright Act, R.S.C. 1970, c. C-30, and subsequent amendments.

AVIS

La qualité de cette microforme dépend grandement de la qualité de la thèse soumise au microfilmage. Nous avons tout fait pour assurer une qualité supérieure de reproduction.

S'il manque des pages, veuillez communiquer avec l'université qui a conféré le grade.

La qualité d'impression de certaines pages peut laisser à désirer, surtout si les pages originales ont été dactylographiées à l'aide d'un ruban usé ou si l'université nous a fait parvenir une photocopie de qualité inférieure.

La reproduction, même partielle, de cette microforme est soumise à la Loi canadienne sur le droit d'auteur, SRC 1970, c. C-30, et ses amendements subséquents.

Canada

THE UNIVERSITY OF ALBERTA

COINCIDENCE MEASUREMENTS OF RELATIVE CROSS SECTIONS FOR $D(\gamma,pp\pi^-)$ IN THE REGION OF THE Δ RESONANCE

BY

MAHER A. F. QURAAN

C

A THESIS

SUBMITTED TO THE FACULTY OF GRADUATE STUDIES AND RESEARCH

IN PARTIAL FULFILMENT OF THE REQUIREMENTS FOR THE DEGREE

OF MASTER OF SCIENCE

IN

NUCLEAR PHYSICS

DEPARTMENT OF PHYSICS

EDMONTON, ALBERTA

SPRING 1993

National Library
of Canada

Acquisitions and
Bibliographic Services Branch

395 Wellington Street
Ottawa, Ontario
K1A 0N4

Bibliothèque nationale
du Canada

Direction des acquisitions et
des services bibliographiques

395, rue Wellington
Ottawa (Ontario)
K1A 0N4

Your file Votre référence

Our file Notre référence

The author has granted an irrevocable non-exclusive licence allowing the National Library of Canada to reproduce, loan, distribute or sell copies of his/her thesis by any means and in any form or format, making this thesis available to interested persons.

L'auteur a accordé une licence irrévocable et non exclusive permettant à la Bibliothèque nationale du Canada de reproduire, prêter, distribuer ou vendre des copies de sa thèse de quelque manière et sous quelque forme que ce soit pour mettre des exemplaires de cette thèse à la disposition des personnes intéressées.

The author retains ownership of the copyright in his/her thesis. Neither the thesis nor substantial extracts from it may be printed or otherwise reproduced without his/her permission.

L'auteur conserve la propriété du droit d'auteur qui protège sa thèse. Ni la thèse ni des extraits substantiels de celle-ci ne doivent être imprimés ou autrement reproduits sans son autorisation.

ISBN 0-315-82015-2

Canada

THE UNIVERSITY OF ALBERTA

RELEASE FORM

NAME OF AUTHOR:	MAHER A. F. QURAAN
TITLE OF THESIS:	COINCIDENCE MEASUREMENTS OF RELATIVE CROSS SECTIONS FOR $D(\gamma,pp\pi^-)$ IN THE REGION OF THE Δ RESONANCE
DEGREE:	MASTER OF SCIENCE
YEAR THIS DEGREE GRANTED:	1993

Permission is hereby granted to the University of Alberta Library to reproduce single copies of this thesis and to lend or sell such copies for private, scholarly or scientific research purposes only.

The author reserves all other publication and other rights in association with the copyright in the thesis, and except as hereinbefore provided neither the thesis nor any substantial portion thereof may be printed or otherwise reproduced in any material form whatever without the author's prior written permission.

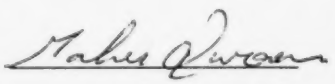

Permanent address:

Hashimi Street,
Bireh, Ramallah,
West Bank.

Date: April 22, 1993.

THE UNIVERSITY OF ALBERTA

FACULTY OF GRADUATE STUDIES AND RESEARCH

The undersigned certify that they have read, and recommend to the Faculty of Graduate Studies and Research for acceptance, a thesis entitled *Coincidence Measurements of Relative Cross Sections for $D(\gamma,pp\pi^-)$ in the Region of the Δ Resonance* submitted by Maher A. F. Quraan in partial fulfilment for the degree of Master of Science in Nuclear Physics.

Dr. N. L. Rodning (Supervisor)

Dr. F. C. Khanna

Dr. W. J. McDonald

Dr. M. Legare

Dr. G. Roy

Dr. E. Korkmaz

Date: April 13, 1993.

ABSTRACT

While early interest in the $\gamma D \rightarrow pp\pi^-$ reaction stemmed from the interest in the $\gamma n \rightarrow p\pi^-$ reaction and hence, focused on the kinematic regions in which the quasi-free process is dominant, more recent interest has been devoted to understanding final state interactions away from this region. Reactions involving few body final states, particularly $\gamma D \rightarrow pp\pi^-$, are the best processes for understanding these final state interactions (FSI). Investigation of these FSI in general and the Δ-N interaction in particular has been limited in the past by the small amount of existing experimental data. Improvements in the duty factor of electron machines and the availability of large acceptance detectors have allowed for a further investigation of such effects covering a large portion of phase space. A recent measurement of the $D(\gamma,pp\pi^-)$ reaction cross section has been performed at the Saskatchewan Accelerator Laboratory (SAL) using the Saskatchewan-Alberta Large Acceptance Detector (SALAD). Preliminary analysis of the data has been performed. Comparisons of the data to microscopic theoretical calculations including different ingredients of the final state interactions as well as the Δ-N interaction are presented.

ACKNOWLEDGMENTS

I wish to express my sincere appreciation to my supervisor, Dr. Nathan Rodning, for his patience, guidance and encouragement. Nathan has provided a great amount of assistance throughout the course of this research. He generously donated his time through many valuable discussions that has greatly improved my understanding of nuclear physics. His comments and suggestions on the previous drafts of this thesis have allowed for a great deal of improvement. The financial assistance received from his research grant is gratefully acknowledged.

I would like to acknowledge all members of the SALAD collaboration at both the University of Alberta and the University of Saskatchewan. Their joint effort has made this project a success. In particular, I would like to thank Dr. Norman Kolb for his various contributions to this project and for reading a previous draft of this thesis, my colleague Evan Hackett for many interesting discussions and helpful remarks, and Dr. Elie Korkmaz for expressing a continued interest in this project and for many helpful comments.

The help of Dr. Faqir Khanna through many discussions on the theory is greatly appreciated. I would also like to thank Dr. J. M. Laget for providing us with the theoretical calculations.

I would like to thank the other members of my defense committee for their helpful remarks. In particular, I would like to thank Dr. John McDonald for reading an earlier draft of this thesis and Dr. Gerald Roy for his helpful remarks.

The help of the Associate Chairman of the Physics Department Dr. Helmy Sherif, the secretary of the Center for Subatomic Research, Llanca Letelier, and the secretary of the physics department, Lynn Chandler, is greatly appreciated.

Table of Contents

Chapter 1: Introduction 1

Chapter 2: Experimental Setup 4

A. Tagged Photon Beam 4
B. Gas Target Cell 10
C. Detector 10
i) Wire Chambers 11
ii) Calorimeter 20
D. Trigger and Data Acquisition 20

Chapter 3: Theory 24

A. Introduction 24
B. The Single Nucleon Term 30
C. Rescattering Effects 37
i) Pion-Nucleon Rescattering 37
ii) Nucleon-Nucleon Rescattering 38
D. The Delta-Nucleon Interaction 42

Chapter 4: Analysis 44

A. Track Reconstruction 44
B. Particle Identification 51
C. Event Selection 60
D. Monte Carlo Simulations 63

Chapter 5: Results and Discussion 67

List of Tables

Table	Description	Page
2.1	Tagging efficiency measurements performed during the $\gamma D \rightarrow pp\pi^-$ experiment	9
2.2	Applied high voltages and measured leakage currents on the four SALAD wire chambers during the $\gamma D \rightarrow pp\pi^-$ experiment	14
4.1	Distribution of track multiplicities found in a typical $\gamma D \rightarrow pp\pi^-$ run.	45

List of Figures

Figure	Description	Page
2.1	Electron Linear Accelerator and Pulse Stretcher Ring (PSR) at the Saskatchewan Accelerator Laboratory (SAL)	5
2.2	Experimental setup for the $\gamma D \rightarrow pp\pi^-$ experiment performed in June 1992	7
2.3	Interrupts-to-tagger sum ratio and electron-to-proton ratio for different collimator (C_1) positions	8
2.4	End view of the SALAD detector	12
2.5	Side view of the SALAD detector	13
2.6	Sum of the charge deposited in the wire chambers for three track $pp\pi^-$ events	15
2.7	Support structure of the wire chambers	16
2.8	Position histogram for the radioactive source located at the center of a wire	18
2.9	SALAD resolution of the scattering angle θ	19
3.1	Total photoabsorption cross section on deuterium	25
3.2	Feynman diagrams for the two body photodisintegration of the deuteron	26

3.3 Total cross sections for single and double pion photoproduction on protons showing the effect of the born terms and the delta resonance 27

3.4 Feynman diagrams for the elementary reaction $\gamma p \rightarrow n\pi^+$ 28

3.5 Feynman diagrams for $\gamma D \rightarrow pp\pi^-$ 29

3.6 Experimental yield for $\gamma D \rightarrow pp\pi^-$ as a function of the spectator nucleon momentum compared to a spectator model calculation 33

3.7 Deviations from the spectator nucleon model at a spectator nucleon momentum of 50 MeV/c 34

3.8 Deviations from the spectator nucleon model at a spectator nucleon momentum of 400 MeV/c 35

3.9 Scattering cross section for $\gamma n \rightarrow p\pi^-$ as extracted from the $\gamma D \rightarrow pp\pi^-$ reaction cross section 36

3.10 Pion exchange Feynman diagrams for $\gamma D \rightarrow pp\pi^-$ 37

3.11 $\gamma D \rightarrow nn\pi^+$ reaction cross section as a function of the pion momentum 40

3.12 $\gamma D \rightarrow pp\pi^-$ reaction cross section as a function of the pion momentum 41

3.13 Feynman diagram for the short range Δ-N interaction 42

4.1 Residuals calculated from the tracking of protons and pions in the SALAD wire chambers for three track $pp\pi^-$ events typical $\gamma D \rightarrow pp\pi^-$ run 46

4.2 A typical reconstructed three track $pp\pi^-$ event as seen in SALAD 47

4.3 Vertex definition for two track events 48

4.4 Minimum distance for three track $pp\pi^-$ events 49

4.5 Radial position of the vertex for three track $pp\pi^-$ events 50

4.6 Z-position of the vertex for events with track multiplicity ≥ 1 from a typical $\gamma D \rightarrow pp\pi^-$ run 52

4.7 θ vs. z plot for events with track multiplicity ≥ 1 from a typical $\gamma D \rightarrow pp\pi^-$ run 53

4.8 Z-position of the vertex for three track $pp\pi^-$ events 54

4.9 Distribution of the azimuthal angle for three track $pp\pi^-$ events 55

4.10 Stopping power as a function of energy for protons and pions as calculated from the Bethe-Bloch formula 57

4.11 Stopping power vs. energy plot for three track $pp\pi^-$ events 58

4.12 Linearized stopping power histogram for three track $pp\pi^-$ events 59

4.13 Kinematic χ^2 distribution for three track $pp\pi^-$ events 62

4.14 p-p elastic scattering cross section at $E_\gamma = 220$ MeV as measured by SALAD 65

5.1 Definitions of the kinematic variables used to describe the $\gamma D \rightarrow pp\pi^-$ reaction 68

5.2 Distributions of $\cos(\theta_\Delta^*)$, $\cos(\theta_\pi^*)$, and ϕ_π^* for three track $pp\pi^-$ events 69

5.3 Feynman diagrams for the Δ-N interaction 70

5.4 Distributions of $\cos(\theta_\Delta^*)$, $\cos(\theta_\pi^*)$, and ϕ_π^* for three track $pp\pi^-$ events for which the $p\pi$ mass is restricted to values below 1110 MeV 72

5.5 Distributions of $\cos(\theta_\Delta^*)$, $\cos(\theta_\pi^*)$, and ϕ_π^* for three track $pp\pi^-$ events for which the $p\pi$ mass is restricted to values between 1110 MeV and 1140 MeV 73

5.6 Distributions of $\cos(\theta_\Delta^*)$, $\cos(\theta_\pi^*)$, and ϕ_π^* for three track $pp\pi^-$ events for which the $p\pi$ mass is restricted to values above 1140 MeV 74

Chapter 1

Introduction

The photodisintegration of the deuteron above the pion production threshold has been of particular interest since the early 1960's. While many experiments on the photoproduction of neutral and positive pions off protons have been performed leading to a good understanding of such processes, experiments on the photoproduction of negative pions off neutrons are scarce. Since construction of neutron targets is not practical, two other methods have been used. The first method is to measure the cross section of the inverse reaction, the radiative pion capture by protons. The dynamics of this process is equivalent to the direct reaction if time reversal is assumed. However, such an assumption could not be taken for granted since the validity of time reversal invariance for such processes had not yet been proved[1].

The other method is to use a deuterium target. Since the deuteron is a loosely bound system, neutrons may be considered to be approximately free. This is known as the spectator model in which the photon is assumed to be completely absorbed by the neutron, while the proton does not participate in the reaction but remains there as a spectator carrying its original Fermi energy and momentum.

Most of the $\gamma n \rightarrow p\pi^-$ cross sections were extracted from the $\gamma D \rightarrow pp\pi^-$ reaction cross sections in the framework of the spectator model. In some cases, cuts were made to exclude regions of the phase space for which deviations from the spectator model are expected to be large. In other cases some of the corrections related to the use of a deuterium target were considered in doing the extraction[1,2,3,4]. The analyses of these experiments are model dependent and since, among other factors, the effects of final state interactions were little known, the controversial results of such experiments were not particularly surprising. Moreover, most of these experiments suffered from at least one of the following experimental limitations:

(1) the use of bremsstrahlung beams which resulted in a relatively large overall uncertainty in the normalization,
(2) poor energy resolutions of about 40-50 MeV, particularly in the bubble chamber experiments,
(3) explorations limited to certain regions of the phase space,
(4) poor statistics and
(5) incomplete determination of final state kinematics.

While early interest in the $\gamma D \rightarrow pp\pi^-$ reaction stemmed from the interest in the $\gamma n \rightarrow p\pi^-$ reaction and, hence, focused on the regions of phase space in which the spectator model might be expected to be valid, recent interest has been devoted to understanding final state interactions away from the region where the quasi-free process is dominant[5,6]. Although photopion production reactions may be induced on heavier nuclei, few body systems and particularly the $\gamma D \rightarrow pp\pi^-$ reaction are the best processes for understanding these final state interaction effects. On the theoretical side, the deuteron wave function is well known, and only three particles emerge in the final state allowing a detailed microscopic calculation. Moreover, photon induced reactions allow for a clean separation between initial and final state interactions. On the experimental side, a coincident measurement can be made such that the final state kinematics are fully determined. Specific final state interactions may then be studied by focusing on certain regions of the phase space where such interactions are expected to produce pronounced effects[7].

In order to study such interactions in more detail, experiments with high statistical accuracy are required for which final state kinematics are completely determined. The difficult task of obtaining a reasonable number of counts is due to the small cross sections of photon-induced reactions which are typically ~1/100 times smaller than those for hadron-induced reactions, and due to the limitation on the photon beams available. Until recently most machines suffered from low tagged photon fluxes (~10^5 Hz) and very small duty factors (<2%). In addition to the difficulty of obtaining enough statistics that such limitations imply, small duty factors result in a reduced signal to background ratio. Moreover, since coincidence experiments are required for a complete determination of final state kinematics, discrete detectors impose serious limitations on statistics.

In the past few years considerable progress was made in improving the duty factors of some accelerators. This caused renewed interest in photonuclear reactions

and raised hopes for a better understanding of such processes. Machines with duty factors up to ~100% include

Saskatchewan (SAL)	E_{max} =	300 MeV
Mainz		855 MeV
NIKHEF		900 MeV
MIT (BATES)		1 GeV
CEBAF		4 GeV.

The experiment described here was performed at the Saskatchewan Accelerator Laboratory (SAL) which has a duty factor over 65%. Outgoing charged particles were detected in coincidence using the Saskatchewan-Alberta Large Acceptance Detector (SALAD). The high duty factor SAL machine and the SALAD detector are described in some detail in the next chapter.

Theoretical calculations may be made using a diagrammatic approach. Each transition amplitude may be expanded in terms of a few relevant Feynman diagrams. This method is analogous to that used in particle physics and is completely relativistic. Appropriate non-relativistic approximations may be made at medium and low energies to simplify the calculations. This method has been used by J. M. Laget in the analysis of final state interactions and has been quite successful in reproducing a large body of experimental data[8]. A detailed description of the calculations is given in the third chapter.

Detailed comparisons of the data to theoretical calculations allow an understanding of final state interaction effects. The calculation may include different ingredients of final state interactions, and the final state kinematics may be chosen so as to focus on the final state interaction of interest. This method has proved to be successful, and several final state interactions have been explored in this fashion. A detailed description of the data analysis is presented in the fourth chapter, and comparisons of the data obtained in the experiment considered here to such calculations are presented in the fifth chapter.

Chapter 2

Experimental Setup

A. Tagged Photon Beam

Pulse stretcher rings (PSR) have been used in the past decade to increase the duty factor of linear accelerators. Duty factors of more than 85% may be obtained using this technique[9]. The earliest PSR successfully achieving high duty factors was designed and built at the University of Saskatchewan, and has been operating since the late 1980's, increasing the duty factor of the linac from 0.03% to over 65%. The experimental program started in the summer of 1988[10].

The pulse stretcher ring of the University of Saskatchewan is 108.78 m in circumference, with an overall length of 50.49 m and an overall width of 6.64 m as dictated by the constraints of a pre-existing building. It consists of two 180° bend regions connected by two straight sections, as shown in figure 2.1. The linac accelerates electrons up to a maximum energy of 300 MeV. The beam is then injected into one of the straight sections of the PSR. The energy of the beam in the PSR is maintained using a radio frequency system. The beam may then be extracted from the straight section opposite to the injection region. The change in tune is achieved through synchrotron radiation losses as electrons pass through the bend regions of the PSR[10,11,12].

For this experiment, technical difficulties resulted in a maximum electron energy of 290.28 MeV, and a reduced duty factor that averaged approximately 44%. The duty factor as a function of time was monitored during each run.

The electron beam travels through the extraction line and passes through a 115 μm aluminum radiator. The electron beam is then momentum analyzed in a magnetic field. Electrons that radiate photons in the selected energy range are bent so as to hit a 62-channel focal plane detector (tagger). The energy of the associated photon is

Figure 2.1 Electron Linear Accelerator and Pulse Stretcher Ring (PSR) at the Saskatchewan Accelerator Laboratory (SAL).

then determined from the radius of curvature of the recoil electron. For an electron of energy, E_e, incident on the radiator, the photon energy, E_γ, is given by

$$E_\gamma = E_e - E_e' \qquad (2.1)$$

where E_e' is the energy of the recoil electron. Electrons that do not radiate are dumped out through an opening in the left side of the experimental area (as seen by the beam) using a sweeping magnet. Lead bricks shielded the focal plane from backgrounds associated with the dumped beam. The experimental setup is shown in figure 2.2.

The photon tagging system consists of the above-mentioned analyzing magnet and a 62-channel focal plane detector. This allows the tagging of photons with energies in the range 187-229 MeV. The tagged energy range may also be changed by changing the magnetic field of the analyzing magnet or the electron energy. The upper limit of 229 MeV tagged photon energy, however, is dictated by the magnet geometry and cannot be exceeded. The tagger provides a photon energy resolution of ~0.6 MeV. Experimental triggers are usually required to occur in coincidence with the tagger. The trigger used in this experiment is discussed in section 2D.

The bremsstrahlung photon beam was collimated using two 12.6 cm long lead collimators of 15 and 20 mm diameter. The horizontal positions of these two collimators are computer controlled. Several tests were performed in order to fine-tune the collimator positions. The best alignment for the first collimator was first determined and the relative position of the second collimator was subsequently determined while fixing the first in place. The best alignment was determined by minimizing the interrupt rate (coincidences between the SALAD detector and the tagger) over the tagger sum ratio while monitoring the electron-to-proton ratio (the best alignment is chosen by minimizing the electron-to-proton ratio as well since background electrons and positrons might be produced off the edge of a collimator). Figure 2.3 shows a typical plot .

A cleaning magnet was placed downstream of the collimators to deflect electrons produced on the collimators. Several trial runs were performed with this magnet off or on. Results showed no improvement in the interrupts-to-tagger sum ratio or in the electron-to-proton ratio with the magnet on. The cleaning magnet was turned off for all $\gamma D \rightarrow pp\pi^-$ runs.

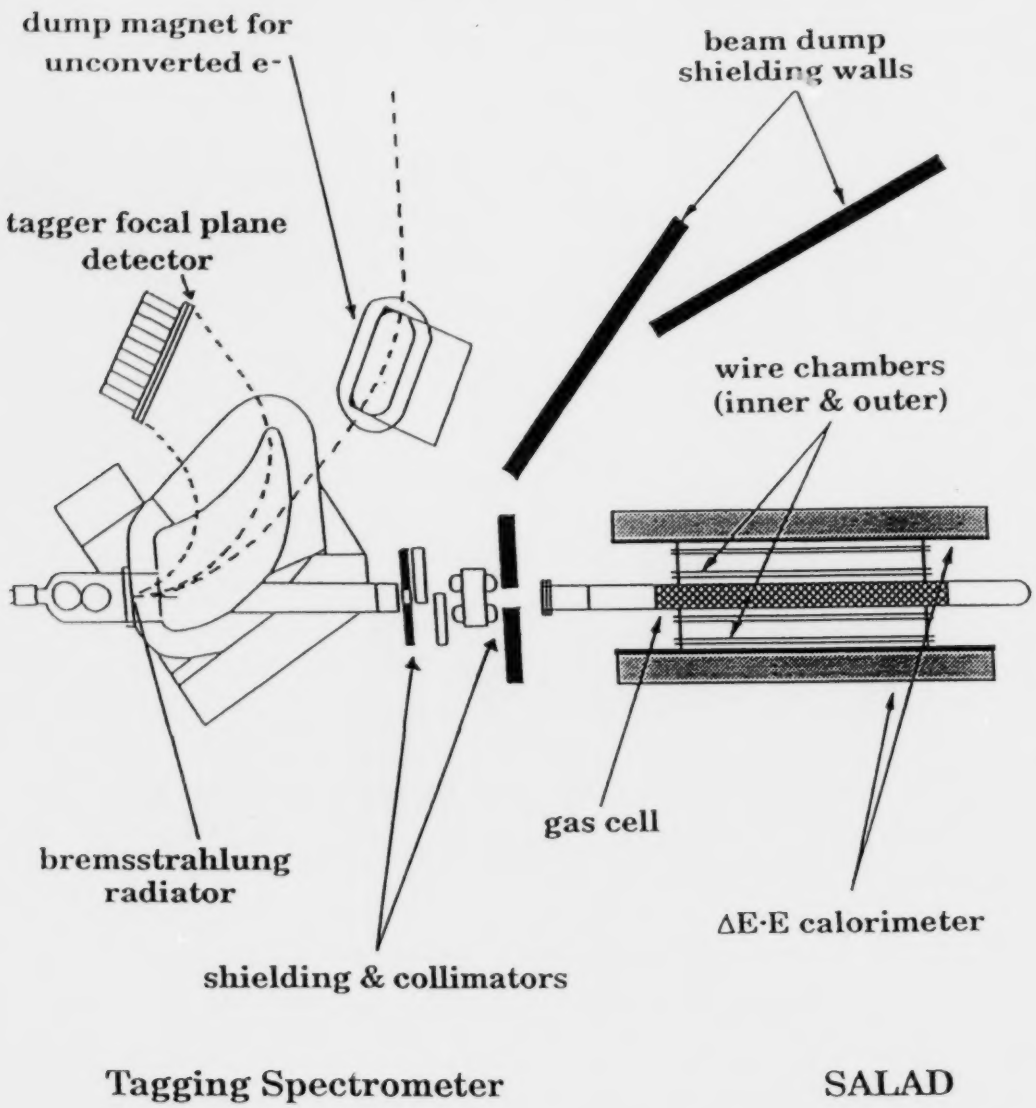

Figure 2.2 Experimental setup for the $\gamma D \rightarrow pp\pi^-$ experiment performed in June 1992.

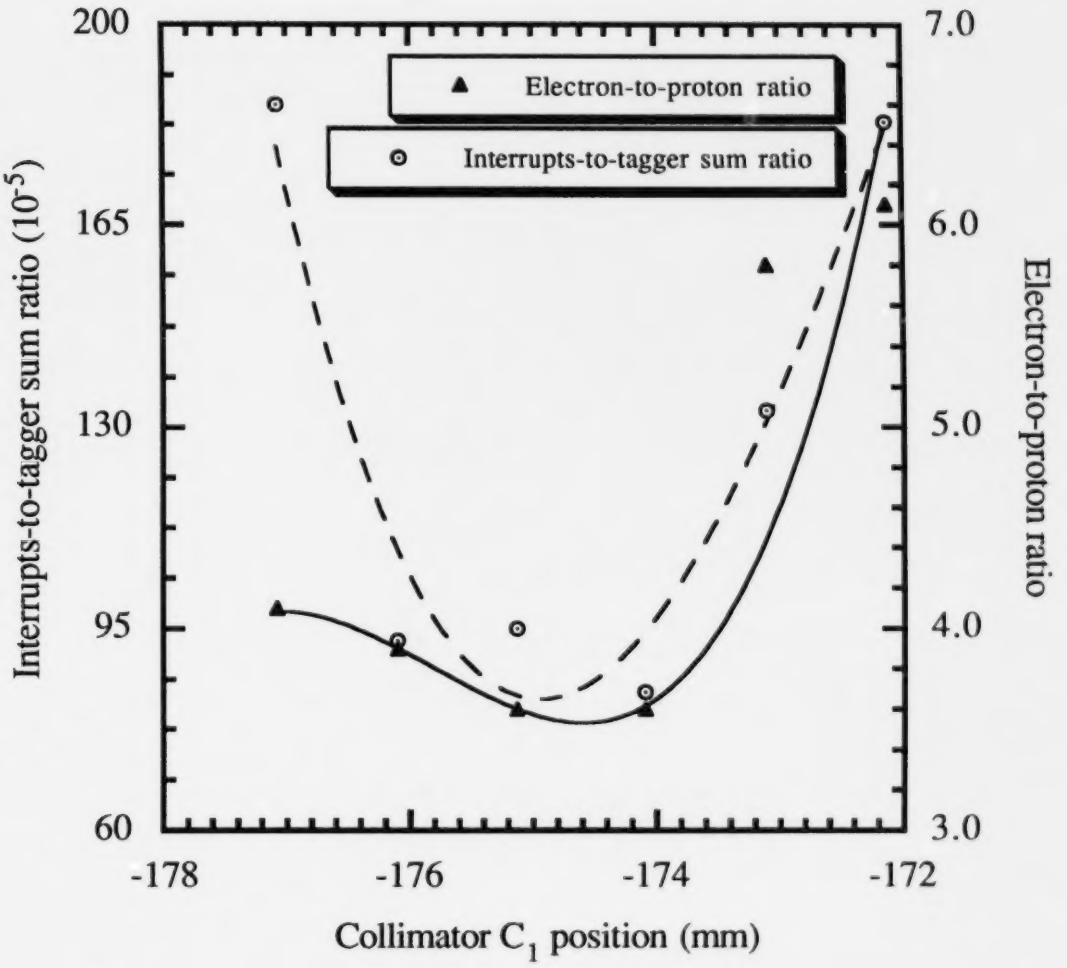

Figure 2.3 Interrupts-to-tagger sum ratio and electron-to-proton ratio for different collimator (C_1) positions.

A lead wall 9 cm thick was placed between the cleaning magnet and the upstream end of SALAD to provide shielding. A third collimator 13.3 cm long of 30 mm diameter was fitted into a hole in the lead wall to allow the beam to pass through. SALAD was aligned so that its axis coincided with that of the beam. A movable lead-glass detector could be placed behind the downstream end of SALAD and was used for tagging efficiency measurements. The cross sectional area of the lead-glass detector was bigger than that of the beam.

In order to determine the incident photon flux, tagging efficiency measurements are required. The incident photon flux cannot be directly determined from the counting rates of the tagger for two reasons. First, background electrons may be detected by the tagger which do not originate from the radiator and hence do not correspond to tagged photons. Secondly, the use of collimators result in cutting part of the photon beam. Electrons that radiate photons may thus be detected by the tagger, while the associated photons may not make it into the target region. The tagging efficiency was measured using the lead-glass detector. The number of tagged photons, N_γ, is measured by requiring a coincidence between the lead-glass detector and the tagger. A background correction is made by repeating the same measurement with the radiator removed. The tagging efficiency, η_{tag}, is then given by

$$\eta_{tag} = \frac{N_\gamma - \left(\frac{\tau}{\tau'}\right) N_\gamma'}{N_{tag} - \left(\frac{\tau}{\tau'}\right) N_{tag}'}, \qquad (2.2)$$

where N_γ is the number of tagged photons with the radiator in, N_γ' is the number of coincidences between the lead-glass detector and the tagger with the radiator removed, N_{tag} (N_{tag}') is the tagger channel sum with the radiator in (out), and τ (τ') is the livetime of the measurement with the radiator in (out). Tagging efficiency measurements are carried out at a much lower photon flux rate than production runs to avoid damage to the lead-glass detector.

Run #	η_{tag} (%)
404	54.4
416	54.9
419	55.2
428	55.4
435	55.7

Figure 2.1 Tagging efficiency measurements performed during the $\gamma D \rightarrow pp\pi^-$ experiment.

After tagging efficiency measurements are made, the high voltage on the lead-glass detector is turned off and the detector is moved away from the beam line under computer control. The tagging efficiencies obtained from some of the tagging efficiency measurements performed during the $\gamma D \rightarrow pp\pi^-$ experiment are given in table 2.1.

B. Gas Target Cell

Small counting rates are expected from photonuclear reactions due to typically small cross sections. A target should therefore be carefully designed so as to optimize the counting rate. Since the counting rate is proportional to the number of target particles per unit area, a large areal thickness would optimize the counting rate. On the other hand, the radial thickness of the target should be small to reduce the energy lost by scattered particles inside the target, and allow such particles to be detected.

The target used in this experiment has an overall length of 237 cm and an inner radius of 5.05 cm. The main portion of the target is made up of 208.3 cm long Mylar lined carbon fiber tubing. Two 33.020 cm long x 0.079 cm thick aluminum tubes are inserted into each end of the fiber tubing. An aluminum dome and an aluminum flange are attached to the downstream and upstream ends of this assembly, respectively. The flange is used to mount a Mylar window. A 60 cm long section of this Mylar lined carbon fiber tubing has been tested without failure to a pressure of 30 atmospheres. In this experiment, the target was filled with deuterium gas at an initial absolute pressure of 6.99 atmospheres. Small amounts of leakage caused the absolute pressure to drop to 6.42 atmospheres at the end of the one week long production run. The target is described in detail elsewhere[13,14].

C. The Detector

An end view of SALAD is shown in figure 2.4. The gas target cell is mounted in the center of the detector with its axis parallel to that of SALAD. The target may be inserted or removed at any time during the experiment. Surrounding the target are two inner wire chambers each containing 36 wires followed by two outer wire chambers each containing 72 wires. The wire chambers are 120 cm long, and are labeled 1 to 4 starting from the innermost chamber. The wire chambers are

surrounded in turn by the calorimeter, an assembly of 24 ΔE-E scintillation counter pairs. The ΔE scintillators are 180.3 cm long and the E scintillators are 182.9 cm long. The overall diameter of the detector is ~75 cm. A side view of the SALAD detector is shown in figure 2.5. The detector's design and calibration are described in detail in references 13 and 14.

i) Wire Chambers

All the wires in the four chambers are aligned parallel to the detector axis. The 36 wires in chamber 1 and 2 are 10° apart. The wires are staggered so that wire #1 in chamber 1 is positioned at a ϕ angle of 10° while wire #1 in chamber 2 is positioned at an angle of 5°. The 72 wires in chambers 3 and 4 are 5° apart. Wire #1 in chamber 3 is at an angle of 5° while that in chamber 4 is at an angle of 2.5°. The wire chambers are used to provide a position determination of passing charged particles.

The chambers operate on the principle of charge division and are operated in the self-quenching streamer (SQS) mode. The chambers are filled with a mixture of 70% isobutane gas (C_4H_{10}) and 30% Argon by volume. Argon provides a high charge gain due to gas multiplication, while isobutane absorbs the ultraviolet photons that cause the discharge to propagate down the wire, thus localizing the position of charge deposition on the wire[18]. The charge deposited is collected at the upstream and downstream ends of the wire. The z-position of the hit is, to first order, linearly proportional to ΔQ, where ΔQ is the difference in the charge collected at the two ends of the wire relative to the total charge. Gain mismatch between the upstream and downstream end electronics require second order corrections. The dependence of z on ΔQ in this case is given by the equation

$$z = L_o + L_1 \Delta Q + L_2 \Delta Q^2 \qquad (2.3)$$

where L_o, L_1 and L_2 are coefficients to be determined from calibration measurements, the details of which are described below.

The walls of the wire chambers are made up of low density polyurethane. This reduces the energy loss of passing particles allowing them to be detected in the calorimeter while avoiding dead zones resulting from the use of supporting rods. This foam is lined on both sides with a thin sheet of Kapton, coated with a conducting film of graphite. The wires in each wire chamber are separated by a thin

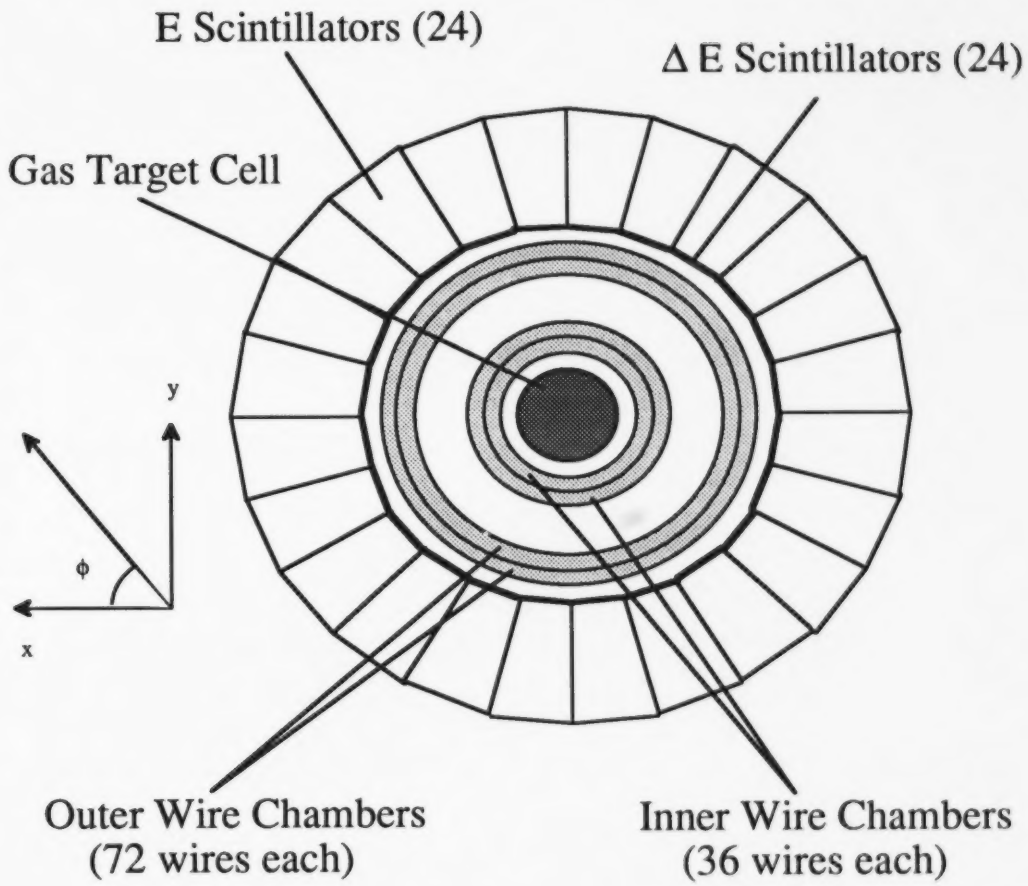

Figure 2.4 End view of the SALAD detector.

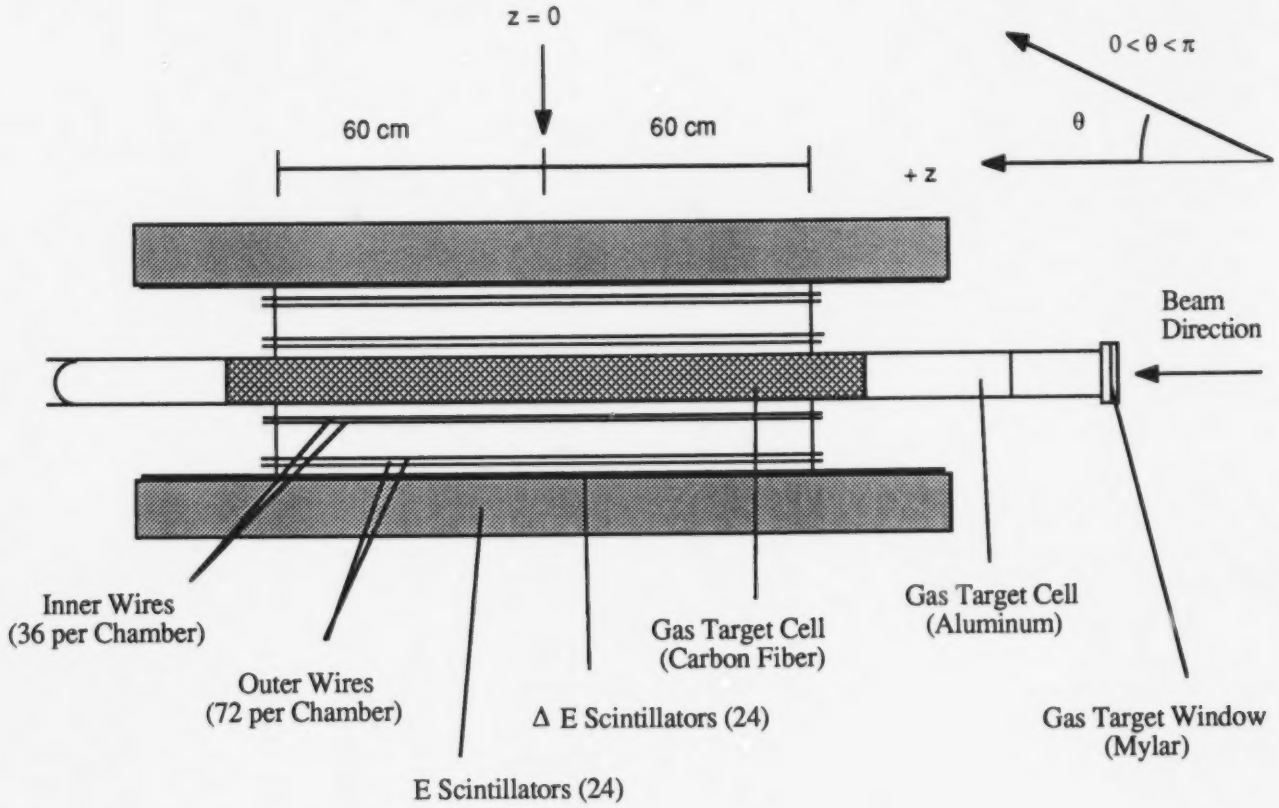

Figure 2.5 Side view of the SALAD detector.

ribbon of graphite coated Kapton. The ribbons and walls are connected to a negative high voltage source. The high voltages that were applied to the wire chambers in this experiment are listed in table 2.2. The correct voltage was determined separately for each chamber from the Q_{sum} spectrum of protons, where Q_{sum} is the sum of the charge collected at both ends of the wires summed for all wires in each chamber. The Q_{sum} for $pp\pi^-$ events for the four chambers at these voltages are shown in figure 2.6.

WC #	HV (kV)	I (μA)
1	- 3.7	~ 90
2	- 3.8	~ 75
3	- 3.9	~ 40
4	- 3.8	~ 50

Table 2.2 Applied high voltages and measured leakage currents on the four SALAD wire chambers during the $\gamma D \rightarrow pp\pi^-$ experiment.

The wires are calibrated using two ^{55}Fe sources located between the inner and outer wire chambers as shown in figure 2.7. One of these sources illuminates the inner chambers while the other illuminates the outer. The sources are well collimated and their positions are computer controlled. When not used, the sources are parked in shielded areas. For a source calibration, the sources are positioned at several z-locations. For each z-position, the sources are rotated around the axis of the detector in steps of 5°. While these sources may not be precisely aligned with respect to one another, the relative positions of the two sources may be determined by tracking cosmic ray particles through the detector. In this way it was determined that in this experiment the two sources were misaligned by -9.5 mm, and this correction was made to the calibration.

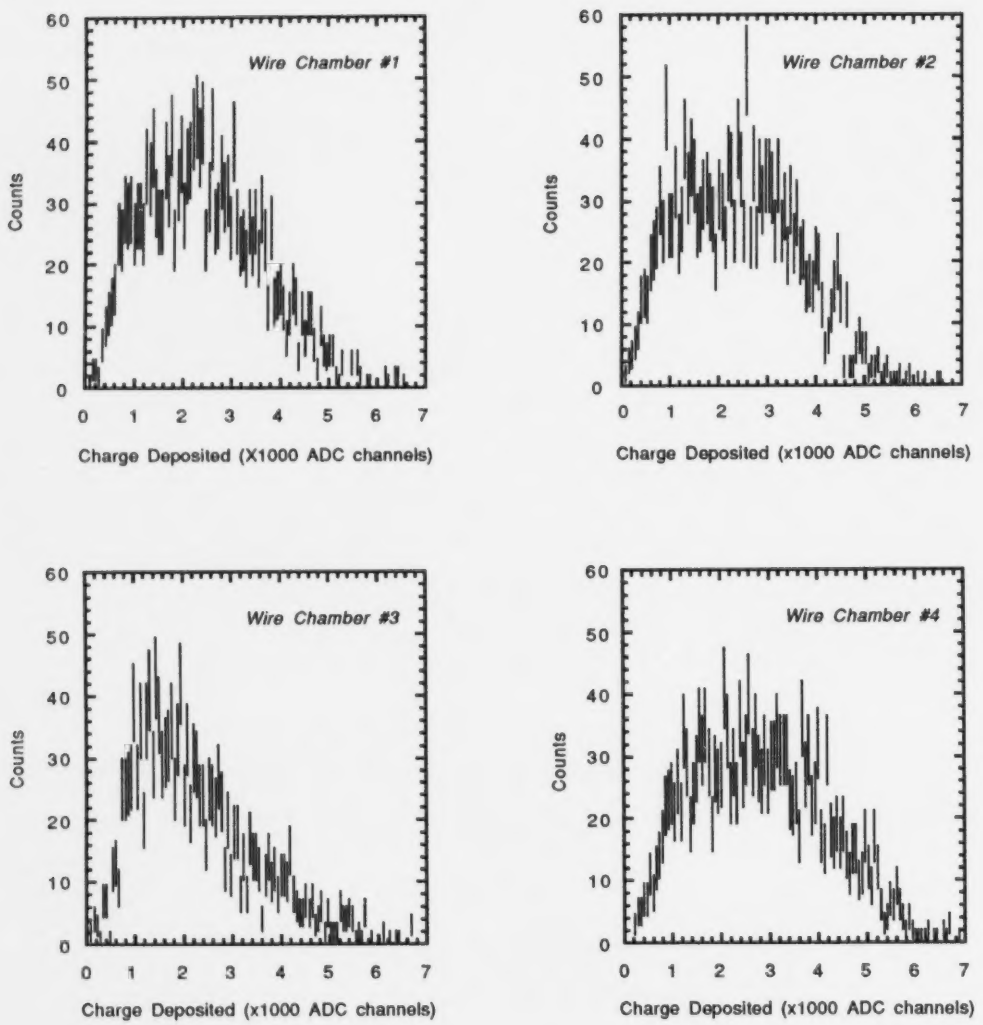

Figure 2.6 Sum of the charge deposited in the wire chambers for three track $pp\pi^-$ events.

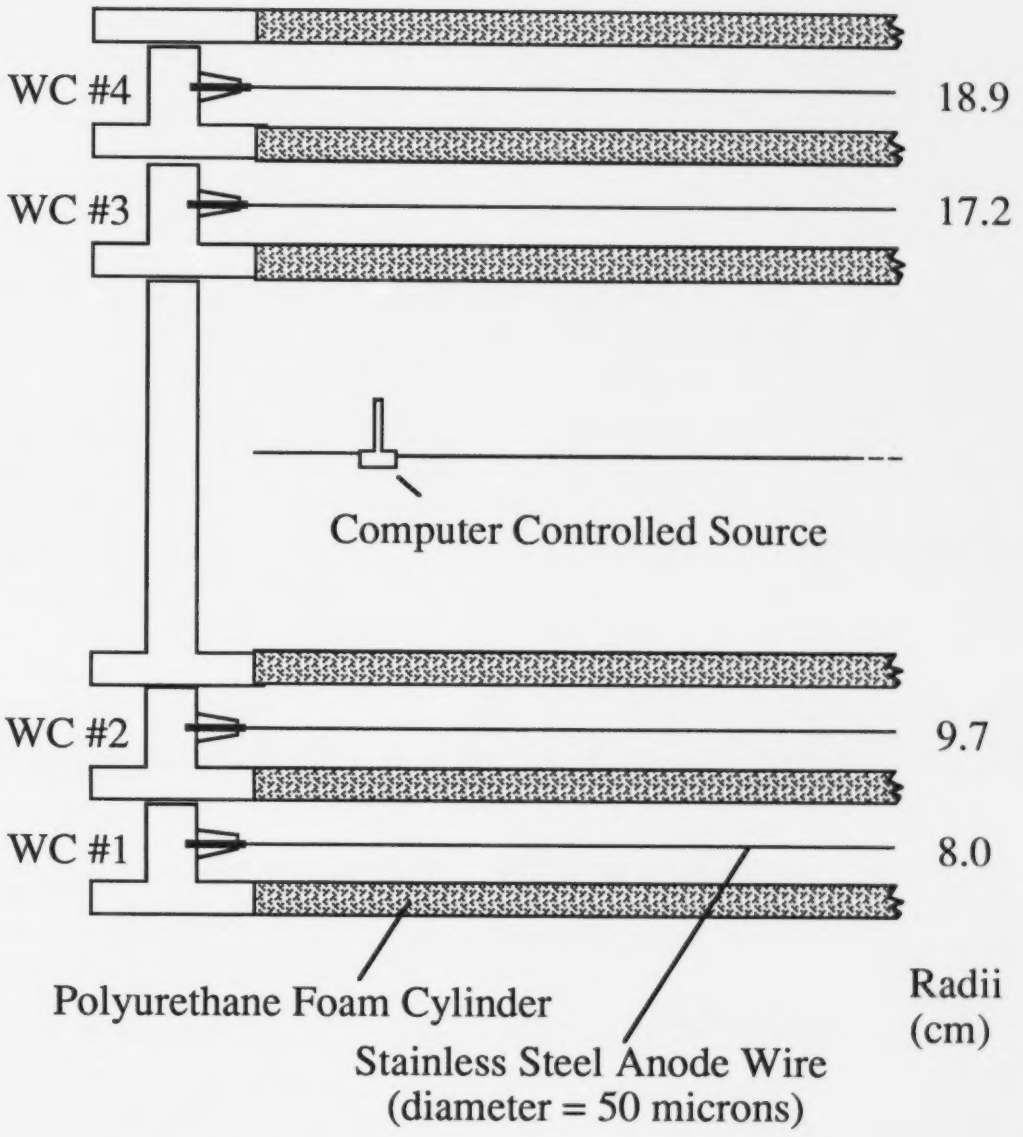

Figure 2.7 Support structure for the wire chambers.

In this experiment two source calibration measurements were made, one before and one after the run. Measurements at seven z-positions were made ($z = 0, \pm 150, \pm 300, \pm 450$ mm). A quadratic fit of z vs. ΔQ was then used to determine the constants of equation 2.3. All source calibration runs performed during a SALAD experiment are typically analyzed and the results compared to ensure that the calibration did not change throughout the experiment. Previous experience has shown that the agreement is quite good. The first of the source calibration measurements was used in the present analysis. The second source calibration will be later analyzed and compared to the first.

For a source run, the trigger is provided by the wire chamber signals. Schmidt triggers are used at both ends of each wire. The two Schmidt triggers are OR-gated. The wires from the four wire chambers are organized in 12 sectors. Each sector contains three wires from each inner chamber, and 6 wires from each outer chamber. The Schmidt triggers in a given sector are enabled only when the wires in that sector are illuminated by the source, and the wires in each sector are OR-gated together. The outputs from these twelve sectors are also OR-gated and sent to the master trigger module.

The wire chambers provide a determination of the coordinates of outgoing charged particles. The finite spacing between the wires limits the ϕ resolution to about $\sigma_\phi = 2.6^\circ$. Two factors limit the z-position resolution in a source calibration measurement. The first factor results from the input impedance of the amplifying circuit. This results in a resolution that is z-dependent; being minimum in the middle and maximum near the ends. The other factor is due to the finite collimation of the source. This results in a resolution of approximately 0.43 mm standard deviation. The overall resolution varies from ~1.2 mm at the center to ~2.5 mm standard deviation near the ends. Figure 2.8 shows a z-position spectrum when the source is located at $z = 0$. Once a charged particle is tracked through the wire chambers, its angle θ may be calculated. The resulting resolution in θ is θ-dependent. Figure 2.9 shows the variation in σ_θ as a function of θ. The z-dependence of σ_θ resulting from the different z-position resolution along the wire is negligible.

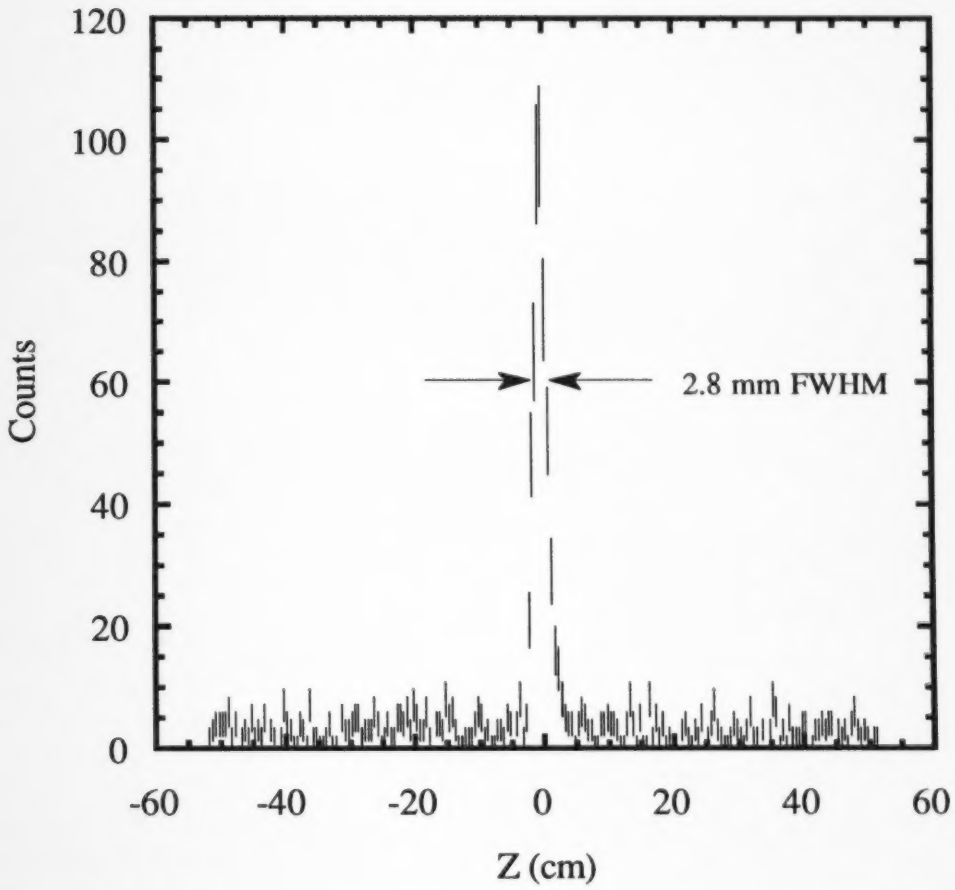

Figure 2.8 Position histogram for the radioactive source located at the center of a wire. The FWHM is 2.8 mm corresponding to 1.2 mm standard deviation.

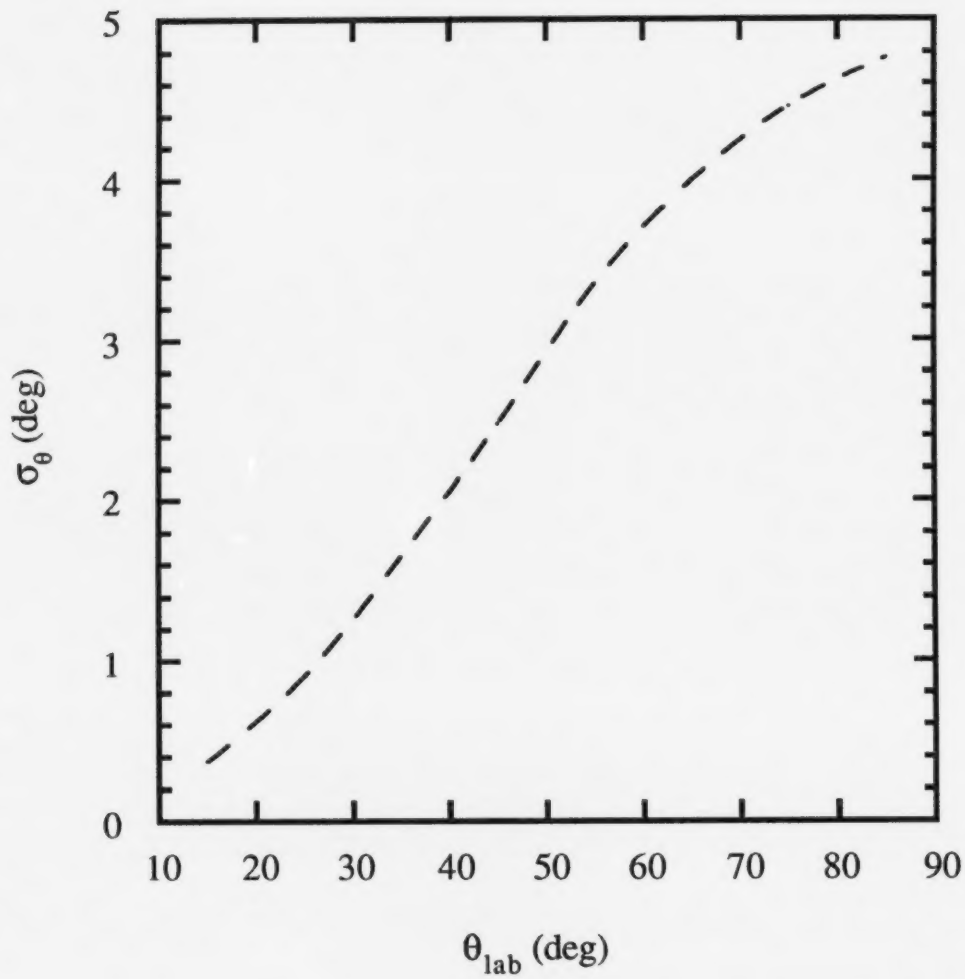

Figure 2.9 SALAD resolution of the scattering angle θ.

ii) Calorimeter

Each of the 24 ΔE-E scintillators subtend an angle of 15° in ϕ. The ΔE scintillators are 0.32 cm thick, while the E scintillators are 12.75 cm thick. The ΔE-E pair can stop pions, protons, and deuterons with energies of 62, 136, and 185 MeV, respectively, incident at 90°. Photomultiplier tubes are attached to both ends of each ΔE and E scintillator via light guides. Since the scintillator bars are 1.83 m long, Bicron BC-408 and BC-412 were chosen for their long attenuation lengths. Each of the ΔE and E scintillators is separately wrapped in a thin sheet of aluminized Mylar. The calorimeter is sealed as a unit by a steel cylinder from the outside and a black vinyl tube from the inside.

Gain calibrations of the ΔE and E PMT's were first determined from p-p elastic scattering at TRIUMF. In two body elastic scattering, a knowledge of the direction of one of the outgoing particles allows a complete determination of the final state kinematics. When a proton is detected, its direction may be determined by tracking it through the wire chambers. Its energy may therefore be calculated, corrected for energy losses in the walls of the target and wire chambers, and compared to the measured ADC value. This allows PMT gain determination. Recent gain measurements were made using experimental data for both $D(\gamma,p)n$ and $^3He(\gamma,pD)$ reactions.

Since gains may change with time, a calibration is required at the time of the experiment. Cosmic rays provide a convenient source of radiation that may be used for this purpose. The energy loss of cosmic rays in the ΔE and E scintillators was measured at TRIUMF after the gains were determined from p-p elastic scattering. This measurement may be repeated at any future time allowing a gain redetermination. Several cosmic runs were made before and after the $\gamma D \rightarrow pp\pi^-$ experiment. One of these cosmic runs was used in the present analysis. The other runs will later be analyzed for comparison.

D. Trigger and Data Acquisition

Two different calorimeter trigger circuits are available. In the first circuit, the four output signals from both the upstream and the downstream ends of a ΔE-E

scintillator pair are sent to a four-fold coincidence unit. Different combinations of these four signals may be computer selected, and the desired thresholds may be demanded.

In the second circuit, the four ΔE-E signals are sent to a Fan in / Fan out module and summed in the form

$$\Delta E_s + f\, E_s \qquad (2.4)$$

where ΔE_s (E_s) is the sum of the upstream and downstream ΔE (E) signals, and f is a constant determined by the signal attenuation and tube gains of the ΔE counters relative to the E counters. This sum may be required to exceed a certain computer selectable threshold refered to as a sum-threshold. The sum-threshold approximates a stopping power discriminator.

The two calorimeter trigger circuits may be used alone or in coincidence. The output from the 24 coincidence units are sent to a 24-input multiplicity logic unit (MLU). This allows triggering on multi-particle final states. The multiplicity is computer selectable and may be set to require anywhere from 1 to 4 ΔE-E scintillator pairs. In a production run, the calorimeter trigger may be required to occur in coincidence with the tagger.

For cosmic runs, since cosmics are minimum ionizing, the first of the above described triggers is used. The selected combination is for $2(E_{upstream} \cdot E_{downstream})$ to be above a reasonably low threshold. For production runs, the sum-threshold is used in coincidence with a $(\Delta E_{upstream} \cdot \Delta E_{downstream})$ trigger. Since the major background at SAL is due to electrons, the sum-threshold allows an on-line rejection of a good fraction of this background, the details of which are discussed in section 4B.

For three particle final state reactions, at least six quantities should be measured for a complete determination of final state kinematics. In the analysis of the $\gamma D \rightarrow pp\pi^-$ reaction a fitting program was used where only over-determined events were analyzed to allow a high confidence level. A minimum of multiplicity 2 trigger was therefore used. The experimental trigger is usually required to occur in coincidence with the tagger. But since the maximum tagged photon energy was 229 MeV, for tagged events, the vertex energy of at least one of the outgoing particles is in most cases too low for that particle to reach the calorimeter and cause a trigger. Many three track events may therefore be lost. To avoid this, the trigger multiplicity

was set such that multiplicity 2 SALAD triggers were required to occur in coincidence with a tagger signal, while multiplicity 3 SALAD triggers were accepted without requiring a tagger signal. This is called a multiplicity 2 + 3 forced trigger. While multiplicity 2 forced trigger was also used for some runs, for the majority of the $\gamma D \rightarrow pp\pi^-$ runs multiplicity 2 + 3 forced trigger was used. Data analyzed here is confined to runs where 2 + 3 forced trigger was required. Preliminary analysis of the multiplicity 2 forced trigger runs shows no substantial increase in the $\gamma D \rightarrow pp\pi^-$ events obtained with this trigger. The threshold was determined from a stopping power histogram. It was chosen to be sufficiently high so that most of the electron background is rejected, but sufficiently low to ensure that few of the pions are being rejected.

A Motorolla VME system was used for data acquisition. The system was first used in this experiment, and resulted in drastically increasing the speed of data acquisition over previous SALAD operation. The limiting factor in the speed of the data acquisition is now the leakage current on wire chamber 1, which imposes a limit on the photon flux. Typical values of the leakage currents on the wire chambers at the wire chamber high voltages for the $\gamma D \rightarrow pp\pi^-$ experiment are listed in table 2.2. The leakage current on wire chamber 1 is highest since this chamber is closest to the beam line, and a large fraction of the background in SALAD occurs at small angles (section 4A). In order to reduce this background and, hence, reduce the leakage currents, a 26.0 cm long, 2.32 cm thick lead shielding tube was designed with an outside diameter of 12.1 cm and was mounted at the upstream end of SALAD. This shielding is removable. While the shielding is expected to reduce the background, a quantitative estimate of this reduction is currently unknown since the shielding was used in all runs due to difficulty in removal.

The rate at which particles are detected in one of the tagger middle channels is called the e-29 rate. The e-29 rate at which the leakage currents cited in table 2.2 were obtained was ~65 kHz. While the wire chambers are expected to withstand higher leakage currents, the e-29 rate was kept at a reasonably low value, such that the leakage current on wire chamber 1 does not exceed ~100 μA. This was mainly done to keep the hit multiplicity reasonably low so that particles may be easily tracked in the wire chambers.

A total of 82 hours of beam on target was achieved. The acquired data were written to magnetic (8 mm video) tapes. About 10% of these data were analyzed on

line and many histograms were monitored during each run. A total of 87 $\gamma D \rightarrow pp\pi^-$ runs were performed, of which 42 were analyzed and are presented here. A typical $\gamma D \rightarrow pp\pi^-$ run is 300 MB's long and consists of ~1 million interrupts.

Chapter 3

Theory

A. Introduction

Figure 3.1 shows the total photoabsorption cross section on deuterium. Below 140 MeV only one channel is present; the two body photodisintegration of the deuteron. This channel is dominated by the quasi-free process at low energies (diagram I of figure 3.2). At higher energies the contributions from two nucleon mechanisms (diagrams II and III of figure 3.2) become important, increasing from about 10% below E_γ=10 MeV to about 30% at E_γ=100 MeV. The two nucleon mechanisms include the photoproduction of a pion at one nucleon which is absorbed by the other. Above the pion threshold, the photoproduction of a real pion soon dominates the cross section. At about E_γ=300 MeV the two body photodisintegration channel accounts for only about 5% of the total photoabsorption cross section. In this energy region the pion resonates with one nucleon to create a $\Delta(1236)$. The delta resonance cross section peaks near E_γ=300 MeV, and has a width (Γ) of about 115 MeV. At higher energies other nucleon resonances are present, but their contributions to the cross section are relatively small (figure 3.3)[15] .

Calculations of the cross sections can be done by expanding the transition amplitudes in terms of Feynman diagrams. This expansion is very useful when dealing with few body final states and intermediate energy reactions. Although a multipole expansion is always possible, many multipoles contribute at relatively high energies, making such a calculation more difficult. Moreover, the diagrammatic method allows the study of the modification of the elementary operators in the presence of the nuclear medium. On the other hand, a diagrammatic expansion is practical only if a small set of relevant diagrams may be selected. This selection is possible since most contributions of multi-loop diagrams are small. The method also has the advantage of being completely relativistic. A full relativistic treatment,

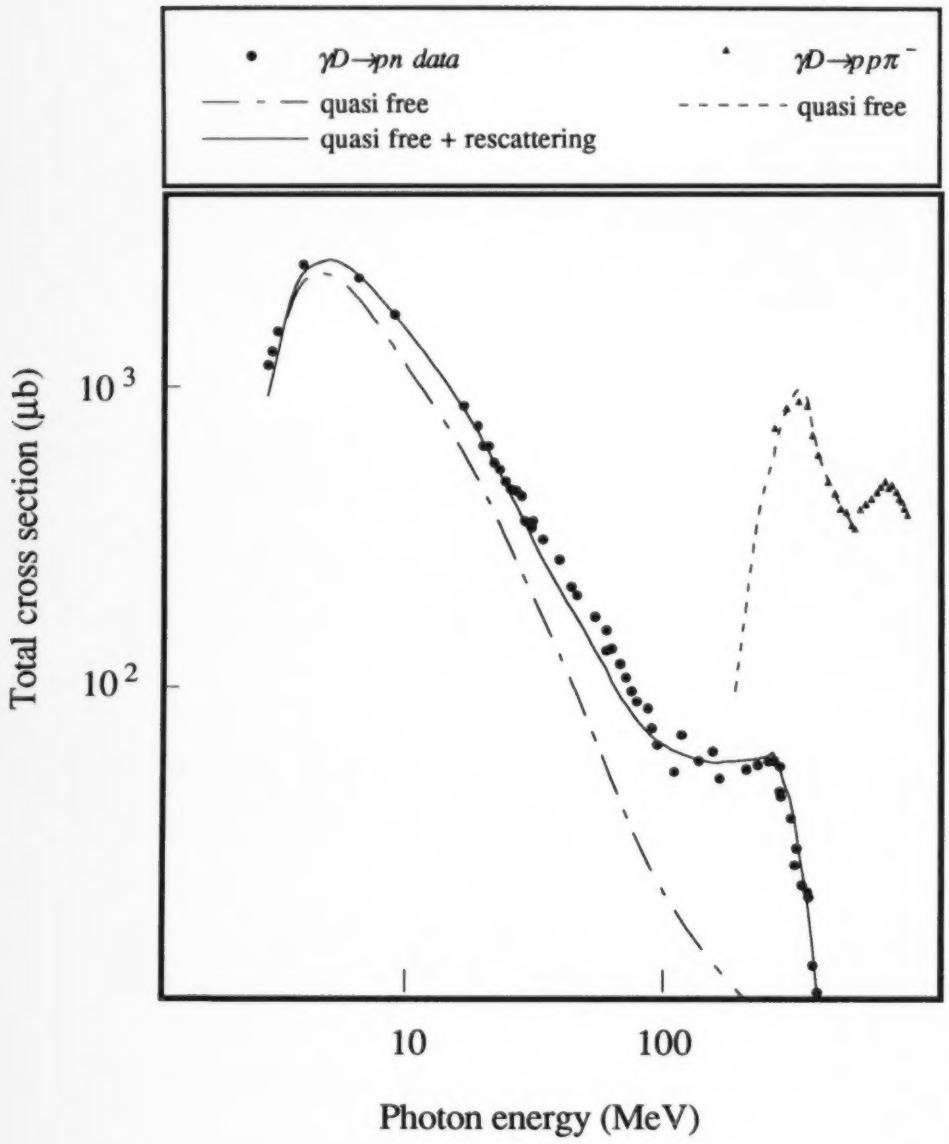

Figure 3.1 Total photoabsorption cross section on deuterium. The experimental data are a compilation from several experiments as plotted in ref. 15. The theoretical curves are calculated by J. M. Laget[15].

however, is not required in the energy range of interest. Since a non-relativistic treatment greatly simplifies the calculations, only terms up to the order p^2/m^2 are retained in the calculation of the transition amplitudes[16].

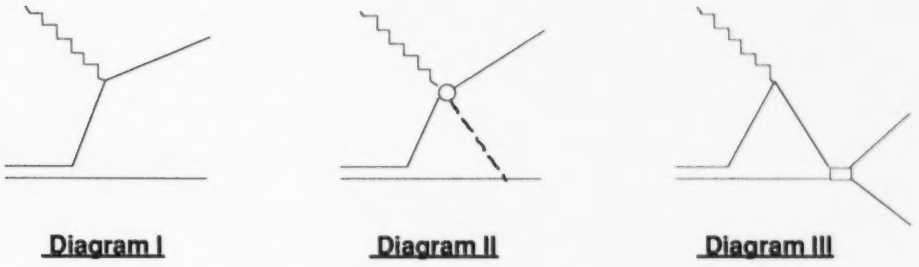

Figure 3.2 Feynman diagrams for the two body photodisintegration of the deuteron.

Each diagram may be expanded in terms of the resonant singularities. This allows each diagram to be singled out and its effects to be examined by choosing the kinematics in the physical region to be close to the singularities. For example, the amplitude of the elementary reaction $\gamma p \rightarrow n\pi^+$ may be expanded in terms of the Born terms and the $\Delta(1236)$ resonance (diagrams I and II of figure 3.4, respectively). The Born terms result in a strong background with little variation with energy, as may be seen in figure 3.3. The amplitude responsible for the creation of the $\Delta(1236)$ has a pole near the mass of the delta and results in the strong variation of the cross section in the corresponding energy range[7].

For the $\gamma D \rightarrow pp\pi^-$ reaction, the diagrammatic expansion is shown in figure 3.5. The kinematic equations for this reaction in the lab frame are

$$\vec{k} = \vec{\mu} + \vec{p}_1 + \vec{p}_2 \qquad (3.1)$$

and

$$k^0 + M_D = \mu^0 + p_1{}^0 + p_2{}^0 \ , \qquad (3.2)$$

where $(k^0,\vec{k})$, $(\mu^0,\vec{\mu})$, $(p_1{}^0,\vec{p_1})$ and $(p_2{}^0,\vec{p_2})$ are the four-momenta of the photon, pion, and the two nucleons, respectively. When a monochromatic beam is used, five independent variables must be measured for a complete determination of the final

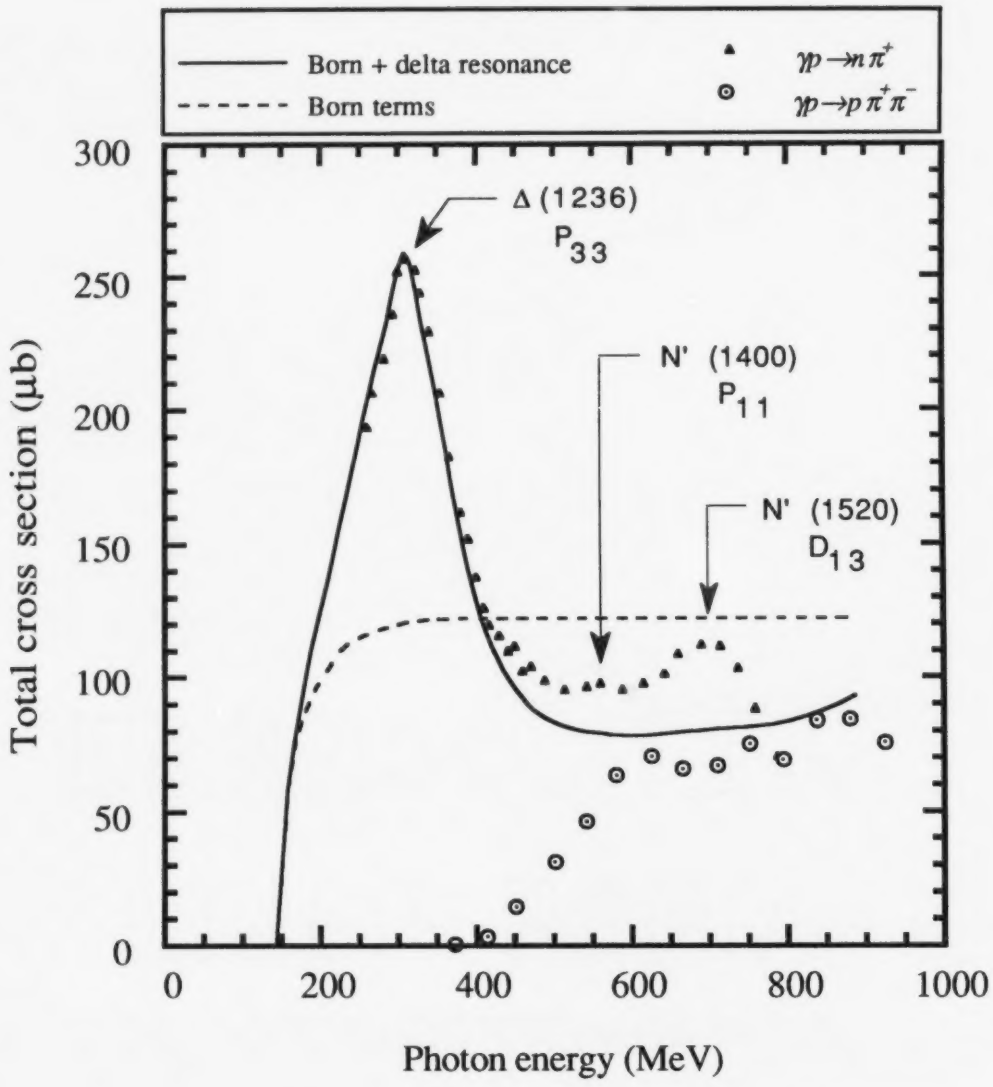

Figure 3.3 Total cross sections for single and double pion photoproduction on protons. The resonances are labeled by their orbital angular momentum L, isospin I, and spin J as $L_{2I,2J}$. The experimental data are a compilation from two experiments as plotted in ref. 7. The theoretical curves are calculated by J. M. Laget[7].

state kinematics. If the measured quantities are the pion momentum and one proton direction ($\mu,\theta_\pi,\phi_\pi,\theta_1,\phi_1$), a measurement of the differential cross section, $d\sigma/d\vec{\mu}d\Omega_1$, is possible. The resulting cross section is[8]

$$\frac{d\sigma}{d\vec{\mu}d\Omega_1} = \frac{Q}{|\vec{\mu}_{c.m.}|} \frac{p_2^0 |\vec{p}_1|^3}{\mu^0 |\vec{p}_1^2 p_2^0 - p_1^0 \vec{p}_1 \cdot \vec{p}_2|} \frac{d\sigma}{d\vec{p}_2[d\Omega_\pi]_{c.m.}} . \tag{3.3}$$

where Q is the total energy of the detected nucleon-pion pair in their center of mass (c.m.) frame. The reduced cross section may be expressed as a sum of the matrix elements corresponding to the six diagrams in figure 3.5[5]

$$\frac{d\sigma}{d\vec{p}_2[d\Omega_\pi]_{c.m.}} = \frac{1}{(2\pi)^5} \frac{|\vec{\mu}_{c.m.}| m^2}{4|\vec{k}| p_2^0 Q} \frac{1}{6} \times$$

$$\sum_{\varepsilon,M,m_1,m_2} \left| \sum_{i=I}^{VI} \mathcal{M}_i(\vec{k},\varepsilon,\vec{\mu},M,\vec{p}_1,m_1,\vec{p}_2,m_2) - \sum_{i=I}^{VI} \mathcal{M}_i(\vec{k},\varepsilon,\vec{\mu},M,\vec{p}_2,m_2,\vec{p}_1,m_1) \right|^2$$

(3.4)

where $\vec{\varepsilon}$ is the photon polarization vector, and M, m_1, and m_2 are the magnetic quantum numbers of the deuteron and the two nucleons, respectively, and m is the nucleon mass. The Pauli exclusion principle is taken into account by subtracting two matrix elements in which the two outgoing protons are exchanged.

Diagram I Diagram II

Figure 3.4 Feynman diagrams for the elementary reaction $\gamma p \rightarrow n\pi^+$.

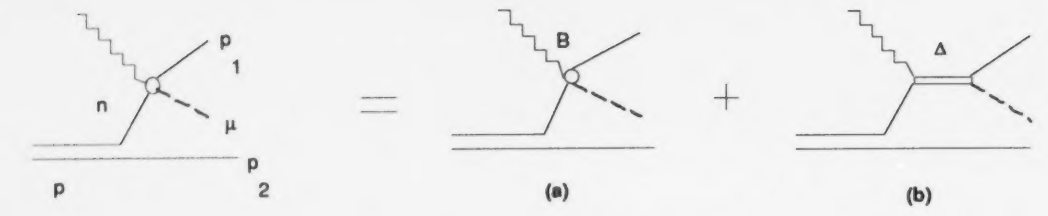

Diagram I

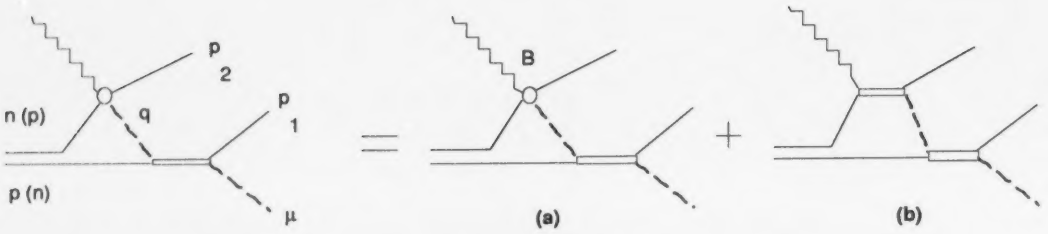

Diagram II

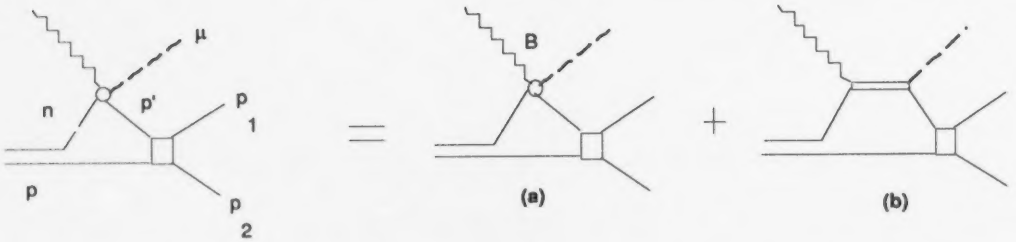

Diagram III

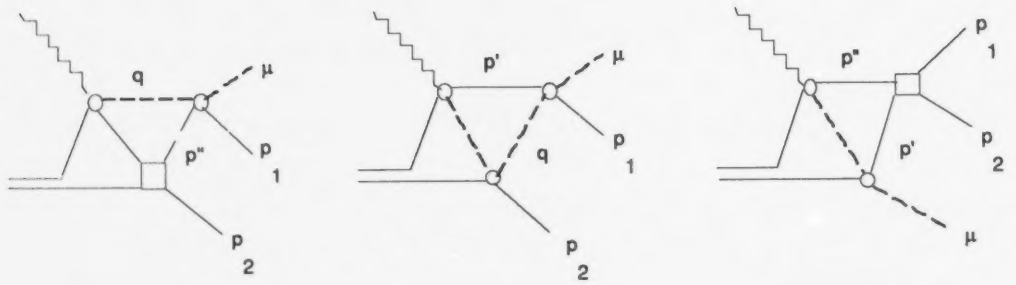

Diagram IV

Diagram V

Diagram VI

Figure 3.5 Feynman diagrams for $\gamma D \rightarrow pp\pi^-$.

B. The Single Nucleon Term

Diagram I of figure 3.5 is the quasi-free diagram. Two vertices appear in this diagram: the $D \rightarrow np$ and the $\gamma N \rightarrow N\pi$ vertex. The $D \rightarrow np$ vertex is defined by the deuteron wave function. The $\gamma N \rightarrow N\pi$ amplitude may be obtained from the transition matrix $T(\gamma N \rightarrow N\pi)$. The resulting quasi-free matrix element may be written as [8]

$$\mathcal{M}_I(\vec{k},\varepsilon,\vec{\mu},M,\vec{p}_1,m_1,\vec{p}_2,m_2) = i \sum_{m_l m_s} \sum_{ls} T_{\gamma N}(\vec{p}_1,m_1,-\vec{p}_2,m_s-m_2) \times$$

$$\langle lm_l sm_s \mid 1M \rangle \left\langle \frac{1}{2}(m_s-m_2)\, \frac{1}{2}\, m_2 \mid sm_s \right\rangle u_l(p_2)\, Y_l^{m_l}(\hat{p}_2), \qquad (3.5)$$

where the deuteron wave function is given by $u_l(p_2)Y_{lm}(p_2)$, and both the s- and the d-wave parts of the deuteron wave functions are allowed. The $T_{fi}(\gamma N \rightarrow N\pi)$ matrix element may be computed and is given up to order p^2/m^2 by

$$T_{fi}(\gamma N \text{ --> } N\pi) = C_\pi C_\gamma \frac{G_1(Q)\, G_3(Q)}{Q^2 - M_\Delta^2 + iM_\Delta \Gamma(Q)} \times$$

$$\left\langle \chi_f \left| \vec{S}.\left[\vec{\mu} - \frac{\mu^0}{M_\Delta}\vec{p}_\Delta\right] \vec{S}^{\dagger} \cdot \left[\left(\vec{k} - \frac{M_\Delta - m}{m}\vec{p}_\Delta\right) \times \vec{\varepsilon}\right] \right| \chi_i \right\rangle, \qquad (3.6)$$

where $\vec{S}$ is a transition spin operator which connects the four component $\Delta(1236)$ with the two component nucleon Pauli spinors, and $\vec{p}_\Delta$ is the total momentum of the pion-nucleon pair. The product of the pionic and the electromagnetic isospin factors are[17]

$$C_\pi\, C_\gamma = \left\{ \begin{array}{ll} \sqrt{2}/3 & \text{for } \gamma n \text{ --> } p\pi^- \\ -\sqrt{2}/3 & \text{for } \gamma p \text{ --> } n\pi^+ \\ 2/3 & \text{for } \gamma p \text{ --> } p\pi^0 \;\&\; \gamma n \text{ --> } n\pi^0 \end{array} \right\} . \qquad (3.7)$$

Two form factors appear in this transition matrix, $G_1(Q)$ and $G_3(Q)$, and should be determined. The width of the delta $\Gamma(Q)$ is allowed to be momentum dependent, and should also be determined together with the delta mass, M_Δ. Three of these parameters, $G_3(Q)$, $\Gamma(Q)$ and M_Δ may be determined by considering $\pi N \rightarrow \pi N$ scattering. The transition matrix for this reaction may be computed using the same method and is given by

$$T_{fi}\,(N\pi \text{ -->} N\pi) = C_\pi^2 \frac{2M_\Delta\, G_3^2(Q)}{Q^2 - M_\Delta^2 + iM_\Delta\Gamma(Q)} \times$$

$$\left\langle \chi_f \left| \vec{S}.\left[\vec{q}_f - \frac{q_f^0}{M_\Delta}\vec{p}_\Delta\right] \vec{S}^{+}.\left[\left(\vec{q}_i - \frac{q_i^0}{M_\Delta}\vec{p}_\Delta\right)\right] \right| \chi_i \right\rangle , \qquad (3.8)$$

where the kinematic equations are

$$q_i^0 + p_i^0 = q_f^0 + p_f^0 = p_\Delta^0 \qquad (3.9)$$

and

$$\vec{q}_i + \vec{p}_i = \vec{q}_f + \vec{p}_f = \vec{p}_\Delta \qquad (3.10)$$

and the pionic isospin factor is given by[8]

$$C_\pi^2 = \left\{ \begin{array}{ll} 1 & \text{for } p\pi^+ \text{ --> } p\pi^+ \ \& \ n\pi^- \text{ --> } n\pi^- \\ 1/3 & \text{for } p\pi^- \text{ --> } p\pi^- \ \& \ n\pi^+ \text{ --> } n\pi^+ \\ \pm\sqrt{2}/3 & \text{for } p\pi^- \text{ --> } n\pi^o \ \& \ n\pi^+ \text{ --> } p\pi^o \end{array} \right\} . \qquad (3.11)$$

The parameters have been determined by fitting the experimental data for $p\pi^- \rightarrow p\pi^-$, $p\pi^+ \rightarrow p\pi^+$ and $\pi^- p \rightarrow \pi^0 n$, and the resulting parameters are as follows[17]

$$M_\Delta = 1231 \text{ MeV}$$

$$\Gamma = 109 \left(\frac{|\vec{q}|}{|\vec{q}_\Delta|}\right)^3 \frac{M_\Delta}{Q} \frac{1 + (R|\vec{q}_\Delta|)^2}{1 + (R|\vec{q}|)^2} \text{ MeV}$$

$$G_3(Q) = \frac{g_3}{m_\pi} \sqrt{\frac{1 + (R|\vec{q}_\Delta|)^2}{1 + (R|\vec{q}|)^2}} \text{ MeV}^{-1}$$

$$R = 0.00552 \text{ MeV}^{-1}$$

$$g_3 = 2.13 , \qquad (3.12)$$

where

$$|\vec{q}| = \frac{1}{2Q}\sqrt{[Q^2-(m+m_\pi)^2][Q^2-(m-m_\pi)^2]} \qquad (3.13)$$

and

$$|\vec{q}_\Delta| = \frac{1}{2M_\Delta}\sqrt{[M_\Delta{}^2-(m+m_\pi)^2][M_\Delta{}^2-(m-m_\pi)^2]}\ . \qquad (3.14)$$

The electromagnetic form factor G_1 may be determined by fitting $\gamma n \rightarrow p\pi^-$ and $\gamma p \rightarrow n\pi^+$ reaction cross section. The value of G_1 is given by

$$G_1 = g_1 \frac{M_\Delta + m}{m}\sqrt{\frac{4\pi}{137}}\ , \qquad g_1 = 0.282\ . \qquad (3.15)$$

When $|\vec{p}_1| >> |\vec{p}_2|$, the antisymmetrization in the quasi-free matrix element, $\mathcal{M}_I$, may be neglected, and the reduced cross section takes the form[8]

$$\frac{d\sigma}{d\vec{p}_2[d\Omega_\pi]_{c.m.}} = \left(1 + \beta_2\cos\theta_2\right)\rho(|\vec{p}_2|)\frac{d\sigma}{[d\Omega_\pi]_{c.m.}}(Q,\omega)\ , \qquad (3.16)$$

where $\rho(|\vec{p}_2|)$ is the momentum distribution of the spectator nucleon, and ω is the angle between the photon and the pion momenta. This is the so-called spectator model, in which the dependence on the spectator nucleon is separated through the factor $(1+\beta_2\cos\theta_2)\rho(|\vec{p}_2|)$. The other factor is the cross section $d\sigma/[d\Omega_\pi]_{c.m.}$ that depends on Q and ω which govern the elementary reaction. This allows a check on the deviations from the quasi-free contribution. As can be seen from figure 3.6, for small values of the spectator nucleon momentum, the agreement is quite good. Deviations start to appear above p_2~200 MeV/c. If Q, ω and $|\vec{p}_2|$ are kept constant, deviations from the quasi-free distribution may be examined by plotting these deviations against the scattering angle of the spectator nucleon[7]. Figure 3.7 shows such a plot at a small value of the spectator nucleon momentum (p_2=50 MeV/c). As expected, deviations at this momentum are quite small. Figure 3.8 shows the same kind of plot at p_2=400 MeV/c, in which case strong deviations are seen[6].

The quasi-free amplitude is adequate in describing the experimental data only for small values of the spectator nucleon momentum (p_2<200 MeV/c). In this region, the elementary reaction $\gamma n \rightarrow p\pi^-$ may be extracted from the $\gamma D \rightarrow pp\pi^-$ reaction cross section in the framework of the spectator model. The data may then be compared to the full calculation of the elementary amplitude as in figure 3.9. This calculation may also be compared to the $\gamma p \rightarrow n\pi^+$ reaction cross section. In both cases the agreement is quite good and yields confidence in the calculation of the elementary amplitude[17]. To account for the final state interactions that take place in the $\gamma D \rightarrow pp\pi^-$ reaction, however, contributions of other diagrams must be considered.

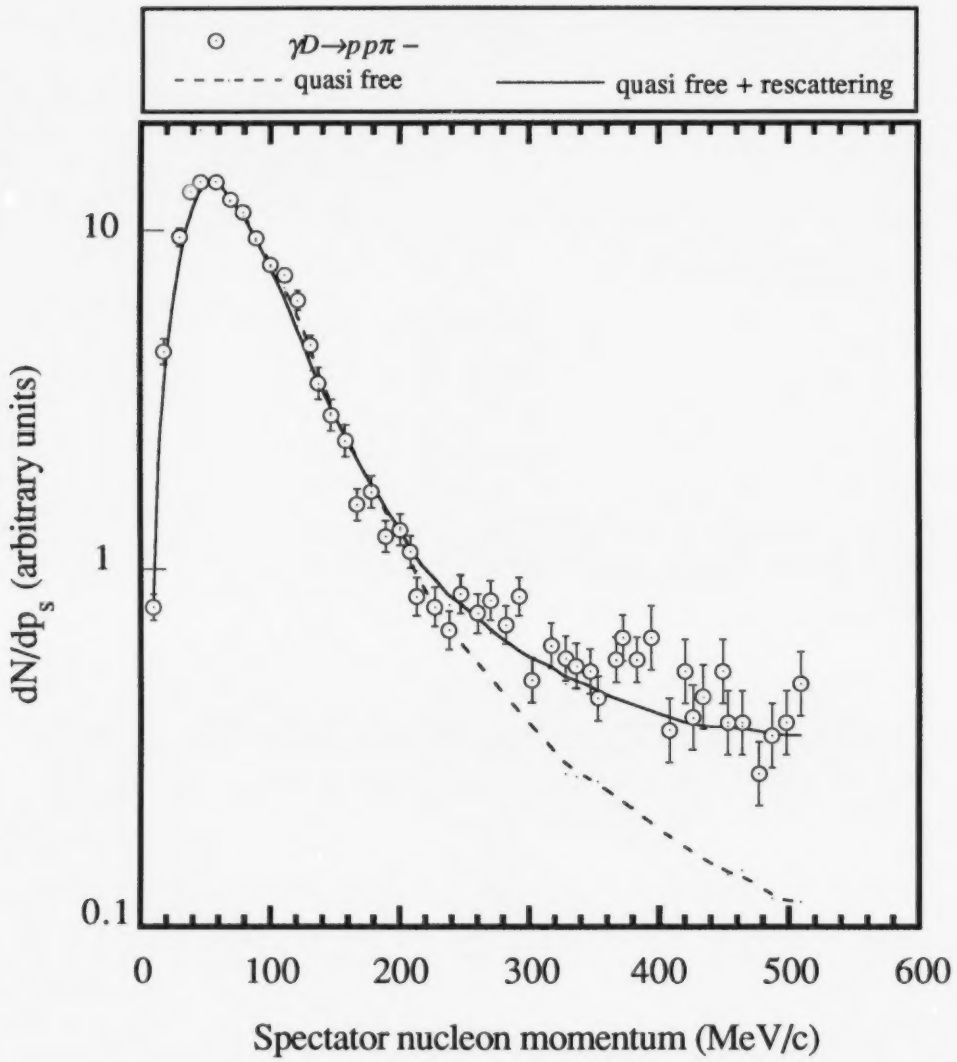

Figure 3.6 Experimental yield for $\gamma D \rightarrow pp\pi^-$. The experimental points are obtained at DESY by Benz. et al.[3]. The theoretical curves are calculated by J. M. Laget[7].

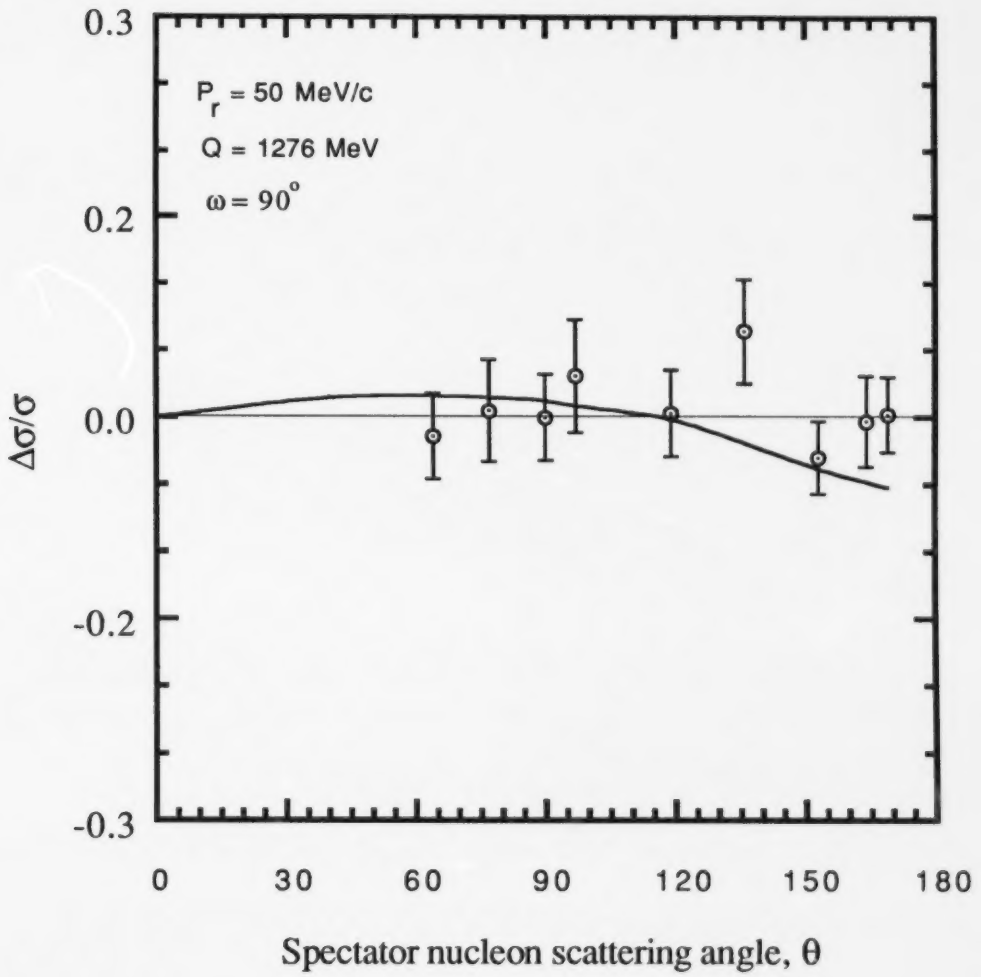

Figure 3.7 Deviations from the spectator nucleon model for $\gamma D \rightarrow pp\pi^-$ at a spectator nucleon momentum of 50 MeV/c. The experimental data are obtained at Saclay by Argan et al.[4]. The theoretical curves are calculated by J. M. Laget[4].

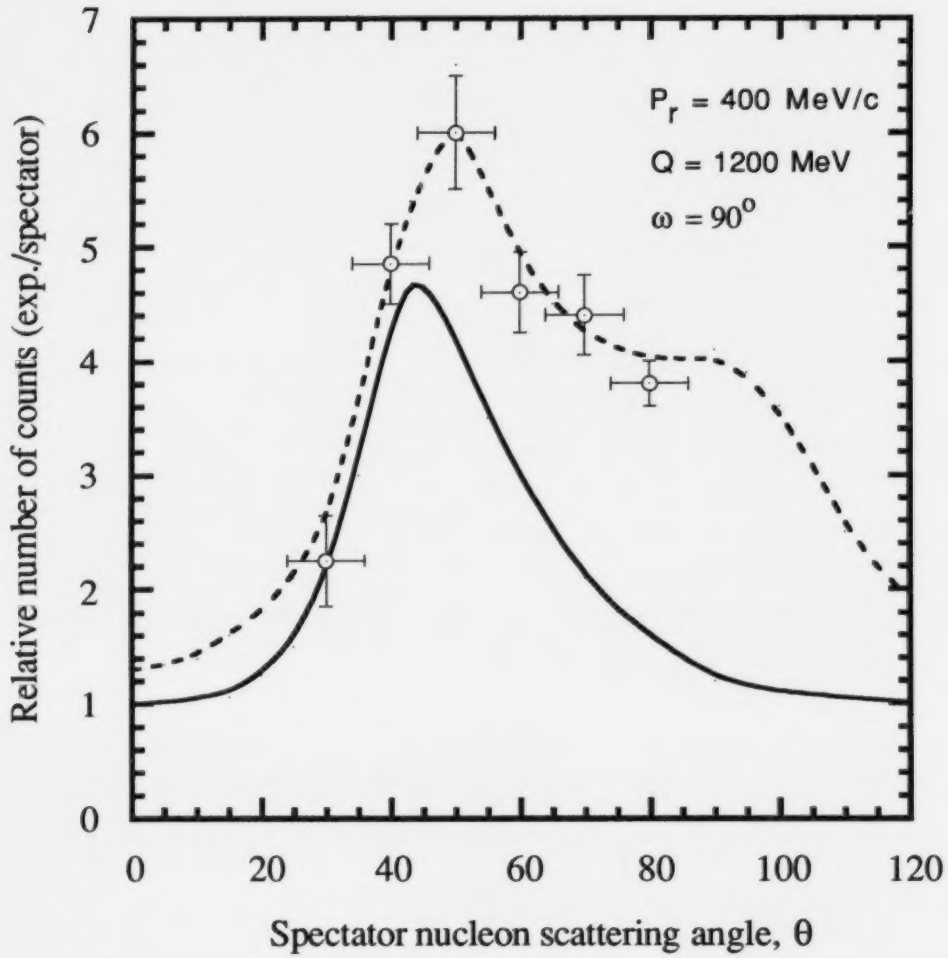

Figure 3.8 Deviations from the spectator nucleon model for $\gamma D \rightarrow pp\pi^-$ at a spectator nucleon momentum of 400 MeV/c. The solid curve includes π-N rescattering, whereas the dashed curve also includes meson exchange currents. The experimental data are obtained at Saclay by Argan et al[6]. The theoretical curves are calculated by J. M. Laget[6].

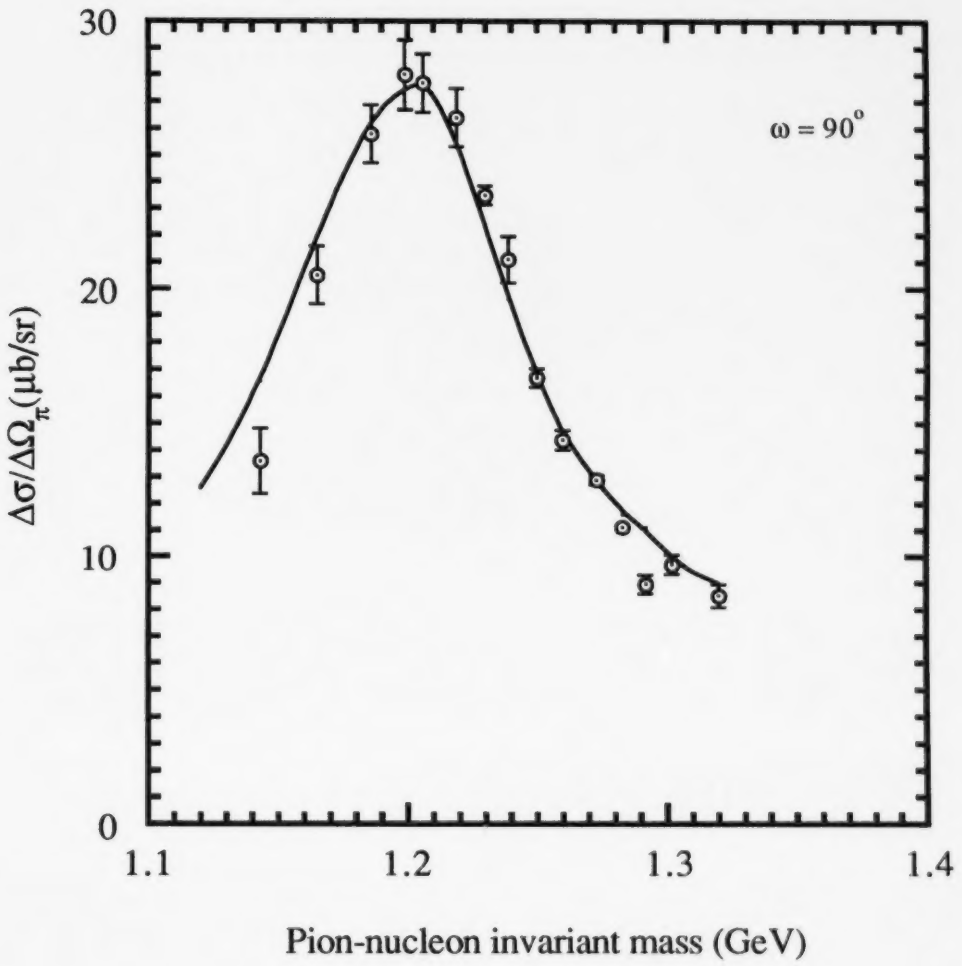

Figure 3.9 Scattering cross section for $\gamma n \rightarrow p\pi^-$ as extracted from the $\gamma D \rightarrow pp\pi^-$ reaction cross section at a spectator nucleon momentum of 50 MeV/c. The experimental points are obtained at Saclay by Argan et al.[4]. The theoretical curves are calculated by J. M. Laget[4].

C. Rescattering Effects

The first contribution to the FSI's to be considered is that of the one loop diagrams. These are the π-N and N-N rescattering effects (diagrams II and III in figure 3.5, respectively).

i) Pion-Nucleon Rescattering

The matrix element for diagram II is given by[8]

$$\mathcal{M}_{II}(\vec{k},\varepsilon,\vec{\mu},M,\vec{p}_1,m_1,\vec{p}_2,m_2) = -i \sum_{m_n,m_p} \left\langle \frac{1}{2} m_n \frac{1}{2} m_p \mid 1M \right\rangle \times$$

$$\int \frac{d^3\vec{p}}{(2\pi)^3} \frac{1}{\sqrt{4\pi}} \frac{u_0(p)\,\widetilde{T_{\gamma N}\,T_{\pi N}}}{q^2 - m_\pi^2 + i\varepsilon}\,, \qquad (3.17)$$

where

$$\widetilde{T_{\gamma N}\,T_{\pi N}} = \left[T(\gamma n \text{ --> } p\pi^-)\,T(\pi^- p \text{ --> } \pi^- p) - T(\gamma p \text{ --> } p\pi^0)\,T(\pi^0 n \text{ --> } \pi^- p)\right] \quad (3.18)$$

to allow for the exchange of charged as well as neutral pions. Three vertices now appear in the diagram: the $D \rightarrow np$, the $\gamma N \rightarrow N\pi$ and the $N\pi \rightarrow N\pi$ vertex identified by the deuteron wave function, $T_{\gamma N}$ and $T_{\pi N}$, respectively. The π-N rescattering amplitude has a singularity near $\theta_2 = 45^0$ which is clearly apparent in figure 3.8. The solid line in the figure includes π-N rescattering effects. Deviations from this calculation may be accounted for by considering meson exchange current corrections. When two pions are produced below the double pion photoproduction threshold, one of these pions is virtual, and is photoproduced at one nucleon and reabsorbed by the other (figure 3.10). This pion is similar to that produced in the photodisintegration of

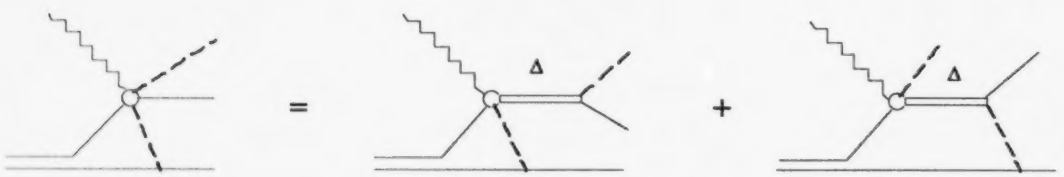

Figure 3.10 Meson exchange Feynman diagrams for $\gamma D \rightarrow pp\pi^-$.

the deuteron below the single pion threshold. Above the double pion photoproduction threshold, the contribution of this mechanism to the total photoabsorption cross section becomes important. As can be seen from figure 3.4, at ~650 MeV the contribution of the $\gamma N \rightarrow N\pi\pi$ channel to the cross section is about 2/3 the contribution of the $\gamma N \rightarrow N\pi$ channel.

The predictions of this pion exchange amplitude are too high unless a form factor is used at each pion-baryon vertex and the exchange of ρ-mesons is allowed. This results in the dashed curve of figure 3.8. The π-baryon form factor is assumed to have the form[15]

$$F_\pi(q_\pi^2) = \frac{\Lambda_\pi^2 - m_\pi^2}{\Lambda_\pi^2 - q_\pi^2} \quad , \tag{3.19}$$

while the ρ-baryon form factor has the form

$$F_\rho(q_\rho^2) = \left[\frac{\Lambda_\rho^2 - m_\rho^2}{\Lambda_\rho^2 - q_\rho^2}\right]^2 \quad , \tag{3.20}$$

where $q_\pi^2(q_\rho^2)$ is the pion (ρ-meson) squared four momentum, and the cut off masses are Λ_π and Λ_ρ for the pion and ρ-meson, respectively. According to a dispersive analysis, the values of these parameters are Λ_π~1 GeV and Λ_ρ=2m, where m is the nucleon mass. This set of parameters lead to a good agreement with the $\gamma D \rightarrow pn$ and $\pi^+ D \rightarrow pp$ reactions as well[8].

ii) Nucleon-Nucleon Rescattering

The matrix element for diagram III (N-N rescattering) is given by[17]

$$\mathcal{M}_{III}(\vec{k},\varepsilon,\vec{\mu},M,\vec{p}_1,m_1,\vec{p}_2,m_2) = i \sum_{m_n,m_p,m_p'} \left\langle \frac{1}{2} m_n \frac{1}{2} m_p \mid 1M \right\rangle \times$$

$$\int \frac{d^3\vec{p}}{(2\pi)^3} \frac{1}{\sqrt{4\pi}} \frac{u_0(p)\left[T(\gamma n \rightarrow p\pi^-)\, T(pp \rightarrow pp)\right]}{p^{0\prime} - E_p' + i\varepsilon} \quad , \tag{3.21}$$

where the third vertex is now due to p-p elastic scattering. The energies $p^{o'}$ and E_p' which appear in the denominator are given by

$$p_0' = E - \sqrt{p^2+m^2} \tag{3.22}$$

and

$$E_p' = \sqrt{(\vec{P}-\vec{p})^2+m^2}\ , \tag{3.23}$$

where

$$\vec{P} = \vec{p}_1+\vec{p}_2 \tag{3.24}$$

and

$$E = p_1^0+p_2^0\ . \tag{3.25}$$

The contribution of the N-N rescattering mechanism becomes important when the relative kinetic energies of the nucleons is small. In the energy range between threshold and a few tens of MeV above threshold, N-N rescattering becomes important, and the cross section is enhanced by up to six times compared to the quasi-free cross section. Figures 3.11 and 3.12 show the contribution of this mechanism at higher energies (E_γ=299 MeV) to the $\gamma D \rightarrow pp\pi^-$ and $\gamma D \rightarrow nn\pi^+$ reactions. When the pion momentum is high, the relative momentum of the nucleons is small and strong effects of the N-N rescattering is apparent. Comparison of the $\gamma D \rightarrow pp\pi^-$ and $\gamma D \rightarrow nn\pi^+$ cross sections in this region show the different contributions of the N-N scattering due to the Coulomb force.

Possible two loop diagrams are also shown in figure 3.5 (diagrams IV, V and VI). The contribution of diagram V has been calculated and found negligible[8]. Diagram VI contributes only in limited regions of the phase space and has been neglected. Only diagram IV is considered. The interaction matrix corresponding to this diagram is given by[8]

$$\mathcal{M}_{IV}\ (\vec{k},\varepsilon,\vec{\mu},M,\vec{p}_1,m_1,\vec{p}_2,m_2) = \int \frac{d^3\vec{p}''}{(2\pi)^3}\ \frac{1}{q^2 - m_\pi^2 + i\varepsilon}\ \times$$

$$[\ \mathcal{M}_{III}^{pp}(\vec{k},\varepsilon,\vec{\mu},M,\vec{p}'',m_p'',\vec{p}_2,m_2)\ T(\pi^-p\rightarrow\pi^-p) +$$

$$\mathcal{M}_{III}^{np}(\vec{k},\varepsilon,\vec{\mu},M,\vec{p}'',m_p'',\vec{p}_2,m_2)\ T(\pi^0n\rightarrow\pi^-p)\ ]\ , \tag{3.26}$$

where an additional factor, $T(N\pi\rightarrow N\pi)$, now appears due to the second loop, and where both neutral and charged pions may be exchanged. The argument that multiple

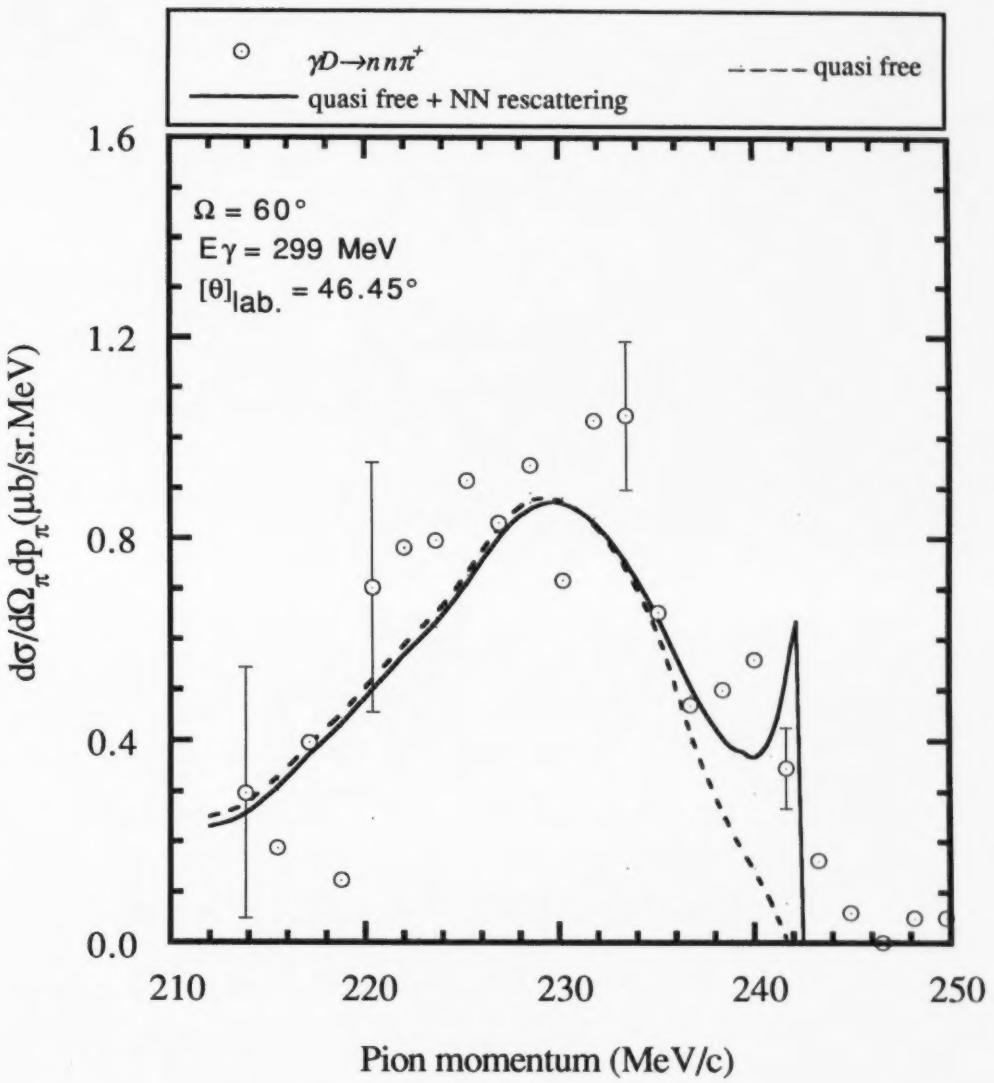

Figure 3.11 $\gamma D \rightarrow nn\pi^+$ reaction cross section as a function of the pion momentum. The experimental points are obtained at Saclay by Ardiot et al. and were taken from ref. 8. The theoretical curves are calculated by J. M. Laget[8].

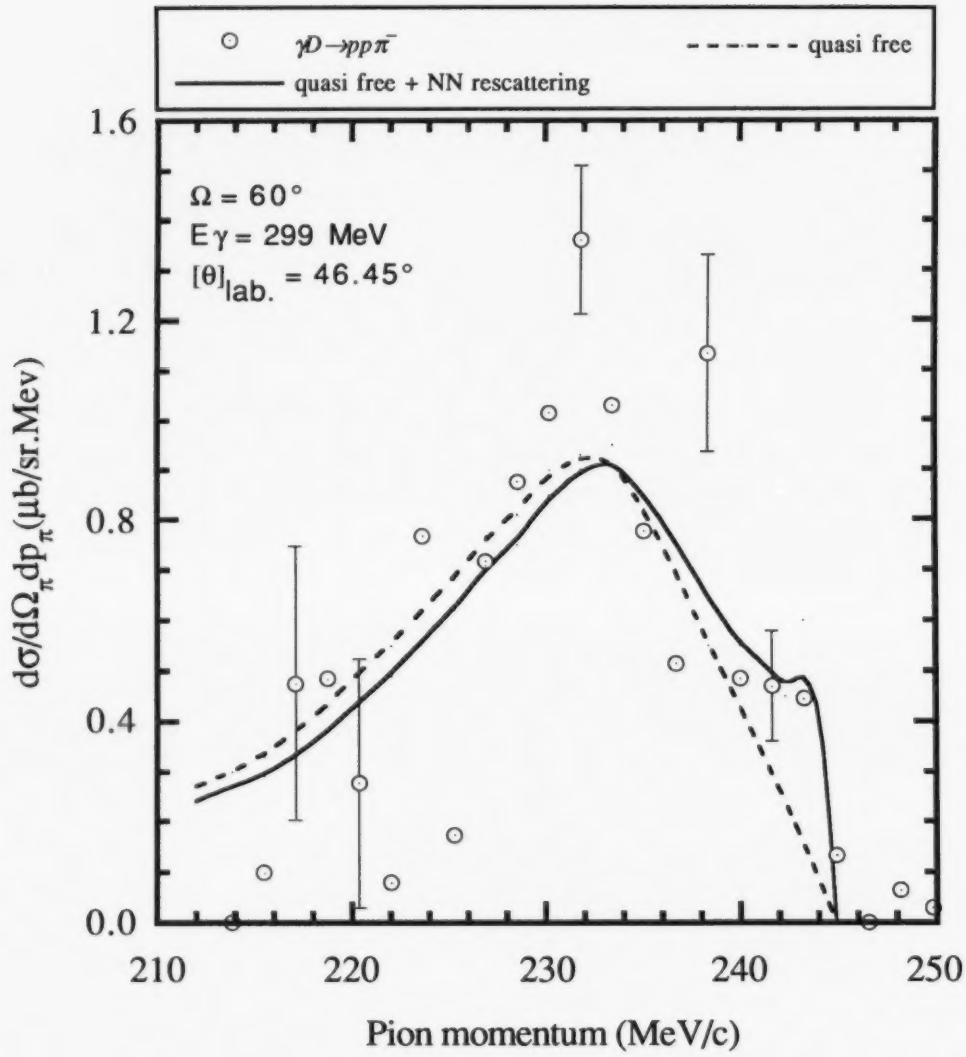

Figure 3.12 $\gamma D \rightarrow pp\pi^-$ reaction cross section as a function of the pion momentum. The experimental points are obtained at Saclay by Ardiot et al. and were taken from ref. 8. The theoretical curves are calculated by J. M. Laget[8].

scattering effects are small is supported by the fact that the behavior of the data are well accounted for by the one loop diagram for both π-N and N-N rescattering.

D. The Delta-Nucleon Interaction

The Δ-N interaction may be divided into two parts: the long range Δ-N interaction which results from the decay of the Δ inside the nucleus, and thus reduces to the multiple scattering effects that have already been discussed. The other part results from the propagation of the Δ inside the nucleus and may be considered as the short-range part of the Δ-N interaction. Comparisons of previous data to a calculation which includes single rescattering effects as well as the two loop diagram discussed above show significant deviations around W_3 =2170 MeV (E_γ=317 MeV) and W_3=2250 MeV (E_γ=415 MeV), where W_3 is the total c.m. three body energy ($W_3=2E_\gamma M_D+M_D^2$)[8].

As previously mentioned, contributions from diagrams with more than two loops are expected to be small and are not expected to account for the observed deviations. In fact, these deviations are far from any dominant singularities in the multiple scattering series. The effect of a Δ−Δ component in the deuteron wave function does not account for the observed deviations. Two other possibilities remain. The first is that the bumps in the cross section at these energies are due to underlying dibaryonic resonances. The second possibility is that the observed deviations are due to the part of the Δ-N interaction which does not reduce to the multiple scattering series. Figure 3.13 shows the Feynman diagram corresponding to this interaction.

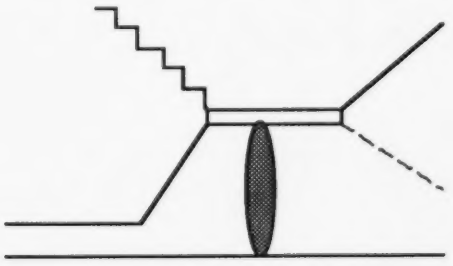

Figure 3.13 Feynman diagram for the short range Δ-N interaction.

The full treatment of the Δ-N interaction requires a solution to the relativistic three body πNN system allowing pion emission and absorption. Only an approximate treatment is considered. Such a solution, although not too accurate, would still help to understand the general nature of the deviations from the multiple scattering series.

When the photon couples directly to the Δ, the delta may rescatter off the spectator proton. If the Δ is treated as a stable particle, an analytic expression may be obtained for the interaction matrix with the same method used to obtain π-N and N-N rescattering effects. The width of the delta is then included by using a Breit-Wigner factor. The photon may also couple to one nucleon and the formation of the Δ may occur through an $NN \rightarrow N\Delta$ transition. Consideration of this channel is very important since interference effects with the Δ-N elastic scattering channel are expected, particularly near threshold.

The structure near the NΔ threshold (W_3=2170 MeV) is better accounted for when the short range Δ-N interaction is considered. Although the agreement is not too good, the calculation shows that the Δ-N interaction is indeed of the same order of magnitude as the deviations from the multiple scattering series, and has approximately the same variation with energy. In fact, good agreement is not expected since several approximations were made in the calculation and not all possible partial waves were considered. This result suggests that a full treatment of the short range Δ-N interaction is likely to account for the structure at W_3 =2170 MeV, and a dibaryonic resonance is not expected. However, this calculation does not account for the structure at W_3= 2250 MeV and the deviations remain to be understood[8].

A possible dibaryonic resonance in the N-Δ final state was also considered. Results from such calculations do not support the existence of dibaryonic resonances at either value. The structure at W_3=2250 MeV, however, does not ascertain the presence of a process different from those considered above. The calculation of the short range N-Δ interaction is too crude to allow for definite conclusions. To be able to draw any valuable conclusions about such deviations, two things are required. On the theoretical side, a complete treatment of the Δ-N interaction is required. On the experimental side, a better understanding of the $\Delta N \rightarrow \Delta N$ elastic scattering is required for which the $\gamma D \rightarrow pp\pi^-$ reaction is best suited.

Chapter 4

Analysis

A. Track Reconstruction

A 'hit' is said to be found on one of the anode wires in the SALAD wire chambers if the sum of the charge collected from both ends of that wire is greater than a set threshold. When two or more hits are found, such that at least one of the hits is in the outer (3 or 4) chambers and at least one is in the inner (1 or 2) chambers, track reconstruction is carried out. The ϕ coordinate of a hit is identified by the position of the wire displaying the hit, whereas the z-position is determined from charge division. The (x,y) position of a hit may then be determined from the known radial position of the wire and the value of ϕ.

The search for wire chamber hits starts from the outer wire chambers. When a hit is found in wire chamber 4 (wire chamber 3), three wires in wire chamber 3 (wire chamber 4) around the wire that displays the hit are searched. If a hit is found, the difference in the z-position of the two hits is determined. If the difference is less than 200 mm, the two hits are assumed to be correlated and the search proceeds to the inner chambers in which wires consistent with a track originating in the target region are searched. This process is repeated until all wires in the outer wire chambers are searched.

The direction of the track, $\hat{\mathbf{t}}$, is defined by the vector sum over all possible vectors, $\mathbf{r}_i$, defined by any two hits

$$\hat{\mathbf{t}} = \frac{\sum_{i>j} (\mathbf{r}_i - \mathbf{r}_j)}{\left| \sum_{i>j} (\mathbf{r}_i - \mathbf{r}_j) \right|} \quad . \tag{4.1}$$

When more than two hits are found in different wire chambers, the track is over-determined and may not pass directly through the points defined by the hits. The minimum distance, d_i, between each hit and the above-defined track is then

$$d_i = \left| \hat{\mathbf{t}} \times \mathbf{v}_i \right| \ , \tag{4.2}$$

where $\mathbf{v}_i$ is a point defined by the hit in a given wire chamber. A tracking residual calculation is then defined such that

$$R = \sum_i \frac{d_i}{N} \ , \tag{4.3}$$

where N is the total number of hits. Residuals calculated from the tracking of protons and pions in the SALAD wire chambers are shown in figure 4.1.

In this analysis the requirement that three tracks be present was imposed. The distribution of track multiplicities per event found in a typical run is shown in table 4.1. Most events have only one track present. The majority of these events result from the large electron background. Imposing a requirement that three tracks be found severely reduces the data set. The reason for this strict requirement will be discussed later. A typical reconstructed three track $pp\pi^-$ event is shown in figure 4.2.

Number of tracks per event	Counts
1	296060
2	283383
3	7591
4	453
5	35
6	4

Table 4.1 Distribution of track multiplicities found in a typical $\gamma D \rightarrow pp\pi^-$ run.

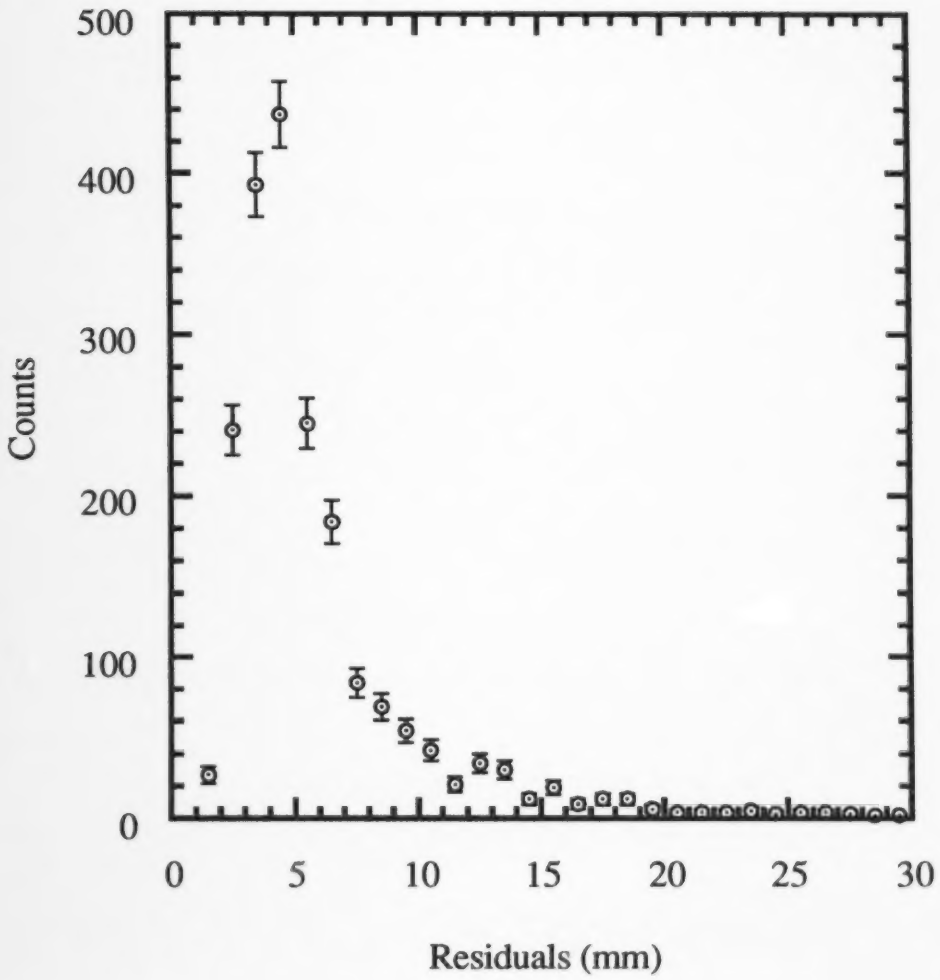

Figure 4.1 Residuals calculated from the tracking of protons and pions in the SALAD wire chambers for three track $pp\pi^-$ events.

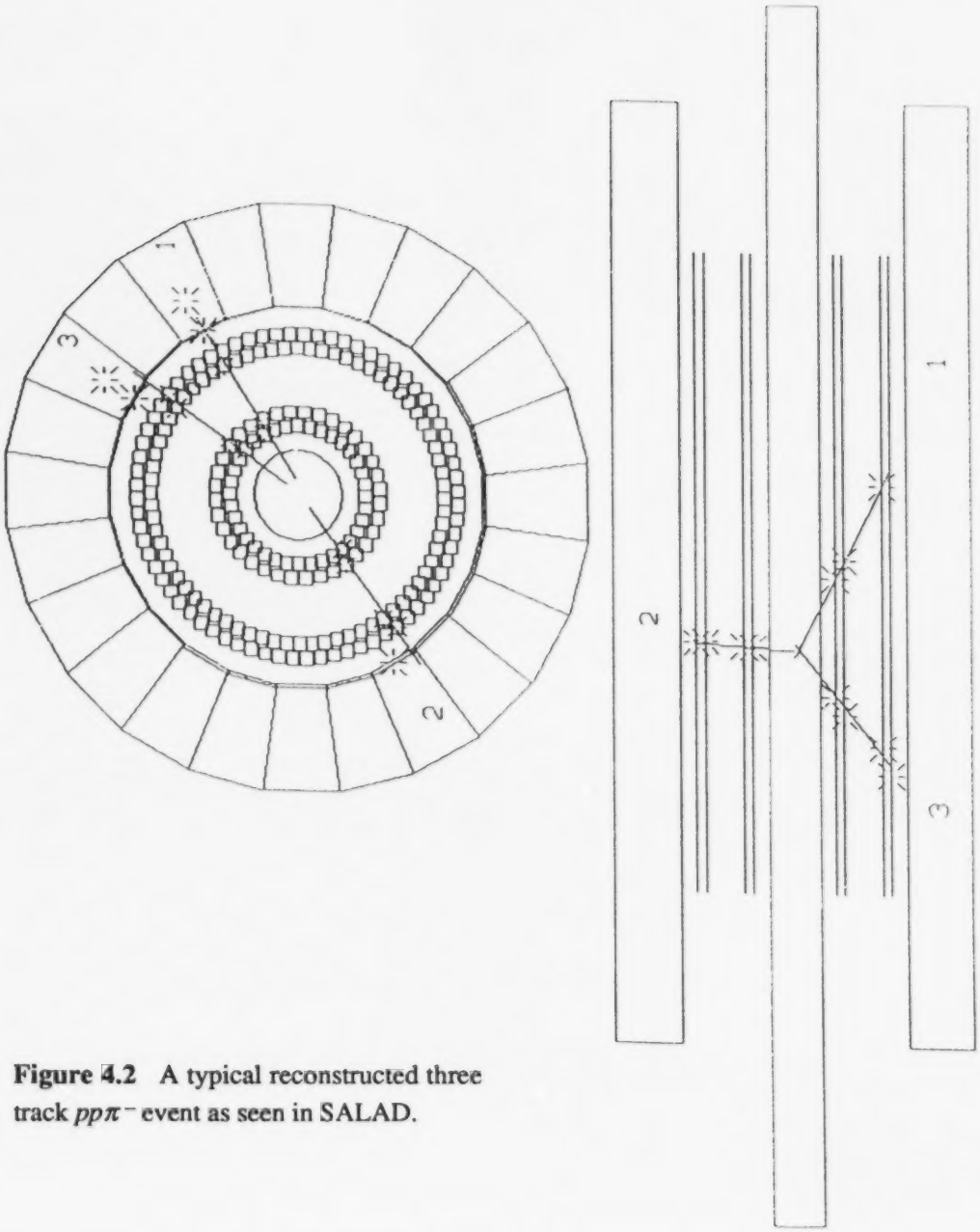

Figure 4.2 A typical reconstructed three track $pp\pi^-$ event as seen in SALAD.

When two or more tracks result from a single event, they should originate from a single point in the target region near the detector axis. Resolution effects result in a non-zero calculated minimum distance between these tracks. When only one track is present, a vertex is defined to be the point on the track closest to the detector axis. For two-track events, the vertex is defined to be the mid-point of the line segment joining the two tracks at their closest approach as illustrated in figure 4.3. When more than two tracks are required, a temporary vertex is defined for the two tracks with the smallest minimum distance as described above. The minimum distances between the other tracks and this temporary vertex are then calculated, and the tracks are considered correlated if this minimum distance is less than 40 mm. The minimum distance between tracks for the event is then defined to be the average of the minimum distances resulting from all possible two track permutations.

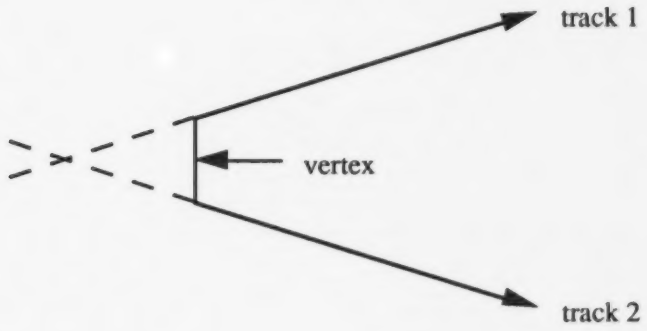

Figure 4.3 Vertex definition for two track events.

The minimum distance and the radial position distributions of the three track $pp\pi^-$ events are shown in figures 4.4 and 4.5, respectively. Cuts were applied to these two values and were chosen to be 40 mm for both the minimum distance and the radial position of the vertex. The z-position of the vertex, z_{vtx}, should be restricted by the target length. A cut was therefore applied such that

$-1200 \text{ mm} < z_{vtx} < 1200 \text{ mm}$

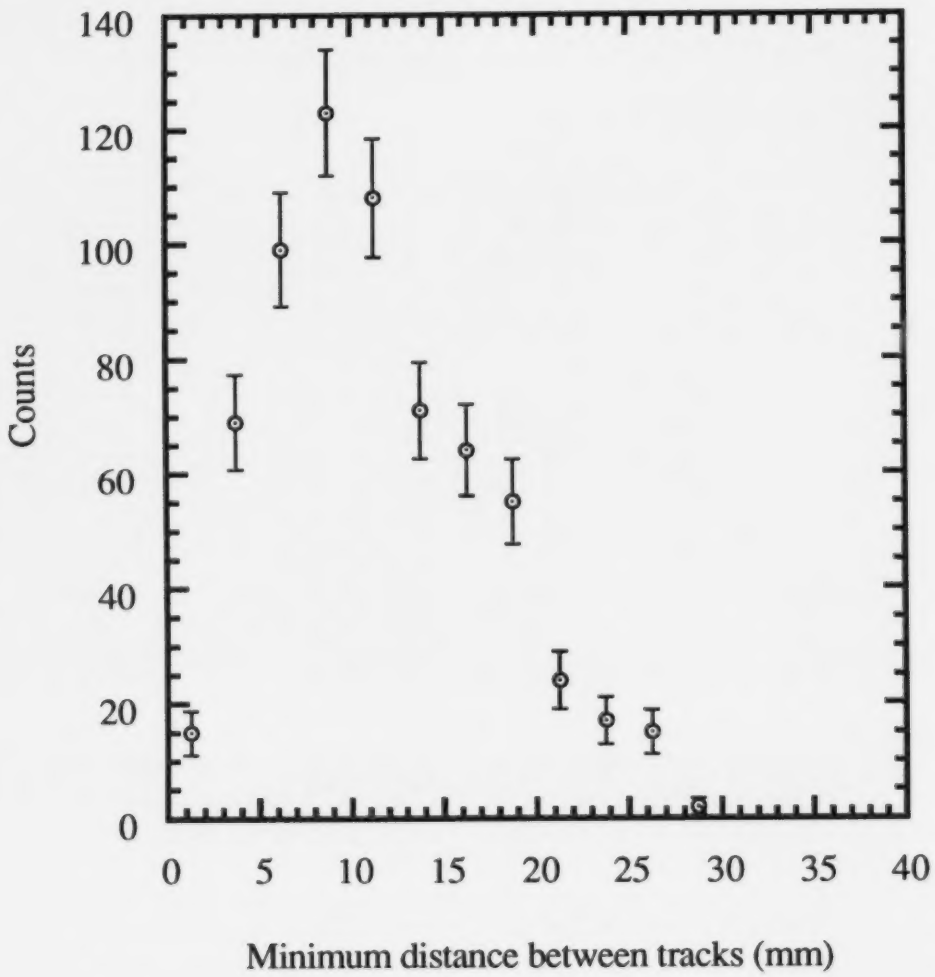

Figure 4.4 Minimum distance for three track $pp\pi^-$ events.

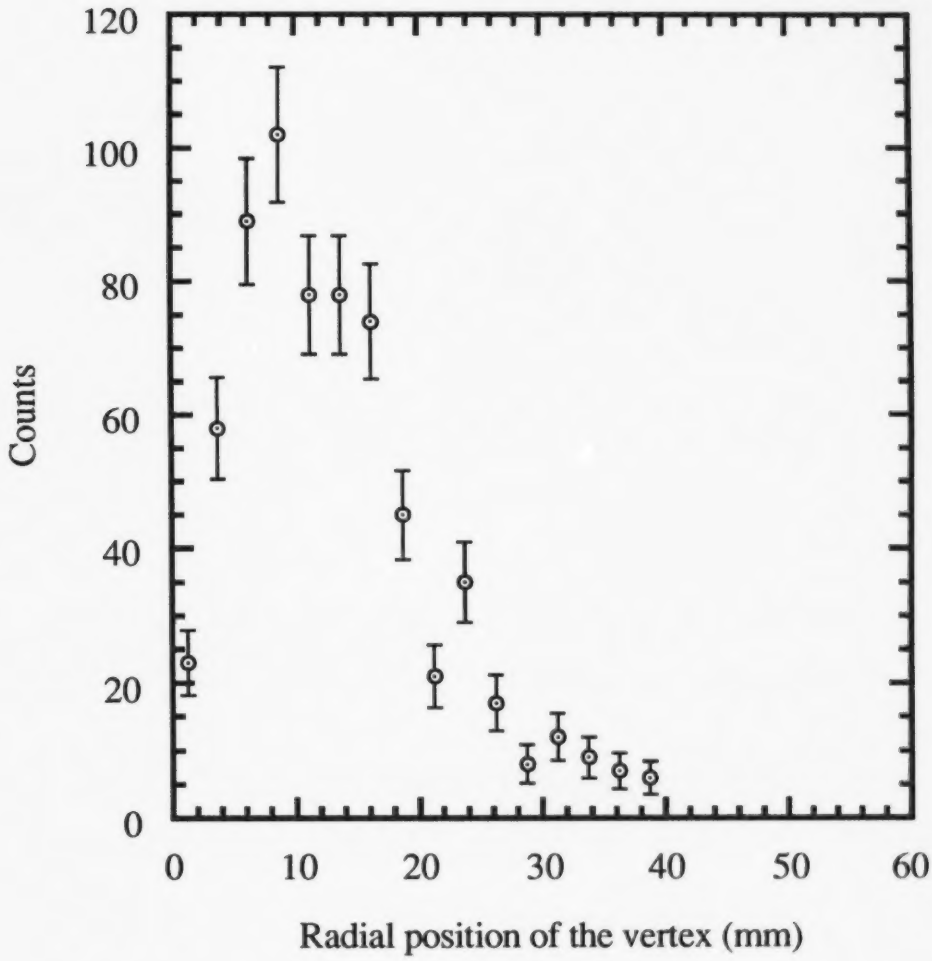

Figure 4.5 Radial position of the vertex for three track $pp\pi^-$ events.

A second cut was also applied on z_{vtx} since a CH_2 target (~2 mm thick) was placed inside the deuterium target. A reasonable cut was determined such that events with z_{vtx} in the range

$$157 \text{ mm} < z_{vtx} < 237 \text{ mm}$$

were rejected. The z-spectrum from a typical run is shown in figure 4.6. The spike is due to events coming from the solid target. The bump at small z values is background. The nature of this background may be clearly seen in the two dimensional histogram of θ vs. z displayed in figure 4.7. In the range of our photon energy, the expected background is mainly due to e^+e^- pair production. Such events have a small opening angle and thus have a better chance of being detected if they originate from the upstream end of the detector. A large portion of this background is rejected once a three track requirement is imposed. The z-position of the vertex for three track $pp\pi^-$ events is shown in figure 4.8.

The azimuthal ϕ distribution for a typical run is shown in figure 4.9. A slight reduction in the number of detected events may be seen in the range 280°- 360°. This is due to the bad performance of one of the wire chambers. Wire chamber 3 was replaced right before this experiment, and tests of the wire chambers prior to the experiment using a statistically significant number of cosmic ray events have shown an uneven distribution in the efficiency of the wires across the new wire chamber 3, reducing down to zero in the above-mentioned ϕ region. A detailed wire by wire analysis for misbehaving wires in all wire chambers will be performed. Events that result from hits on bad wires from any chamber will be rejected in the analysis of real data as well as Monte Carlo simulations.

B. Particle Identification

The energy lost by a particle traversing a given material depends on the charge and velocity of that particle. The energy lost per unit length may be calculated theoretically and is given, to a very good approximation, by the Bethe-Bloch formula[18]

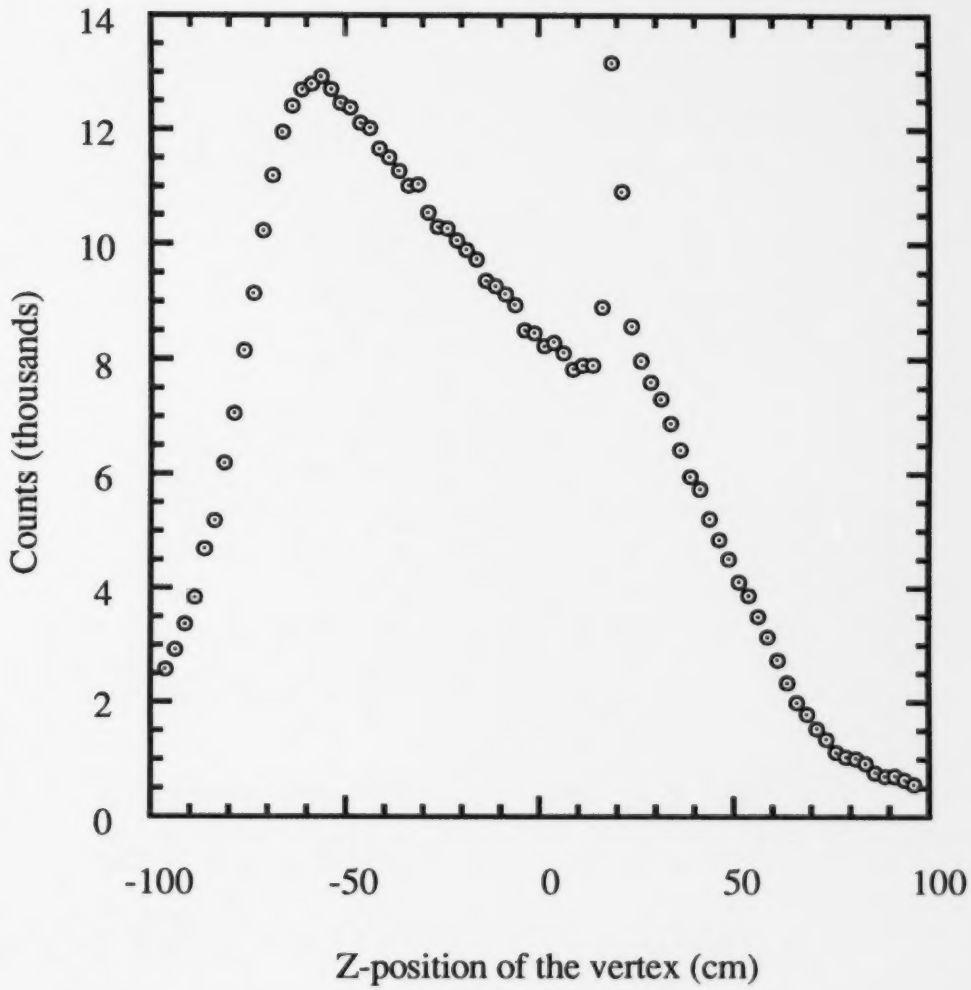

Figure 4.6 Z-position of the vertex for events with track multiplicity ≥ 1 from a typical $\gamma D \rightarrow pp\pi^-$ run.

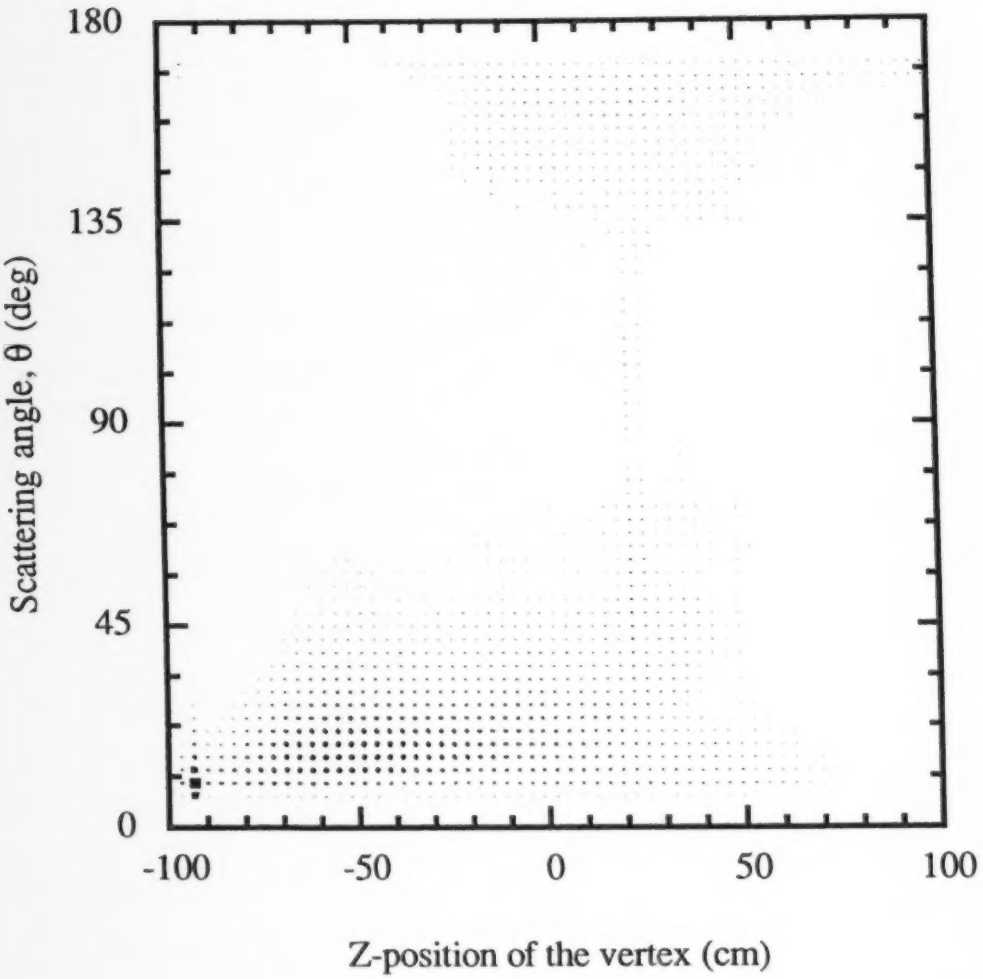

Figure 4.7 θ vs. z plot for events with track multiplicity ≥ 1 from a typical $\gamma D \rightarrow pp\pi^-$ run.

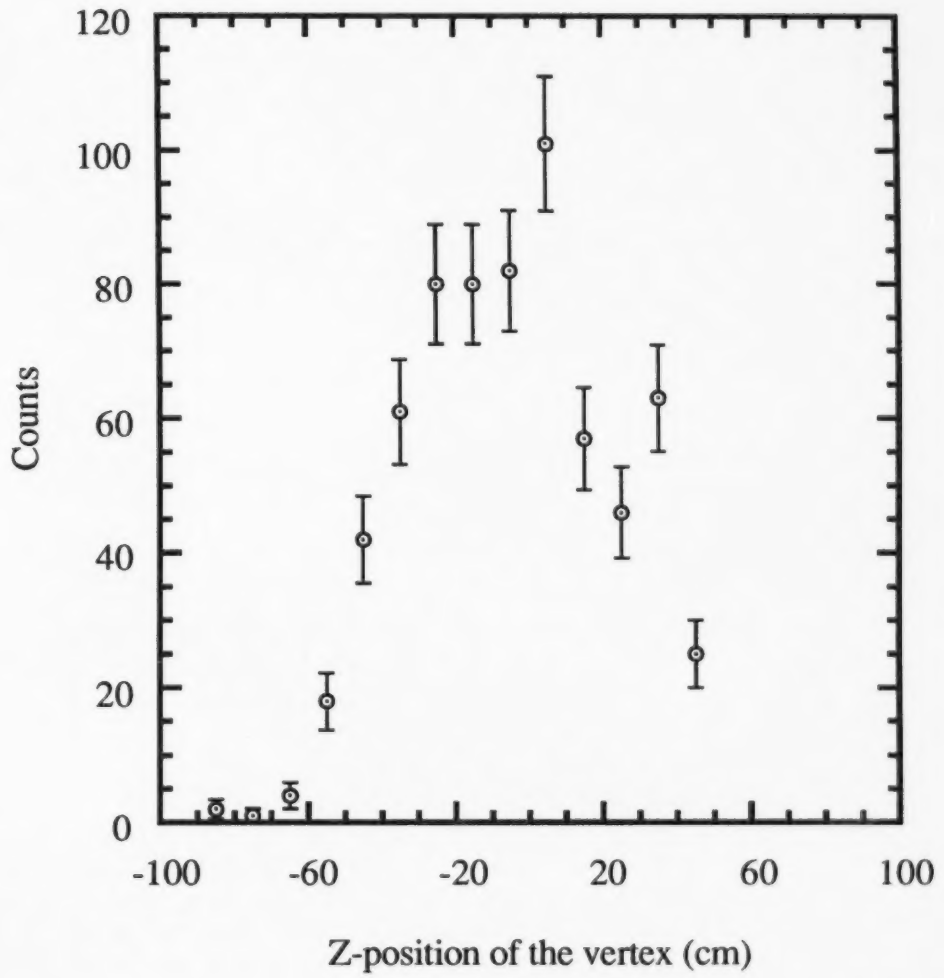

Figure 4.8 Z-position of the vertex for three track $pp\pi^-$ events.

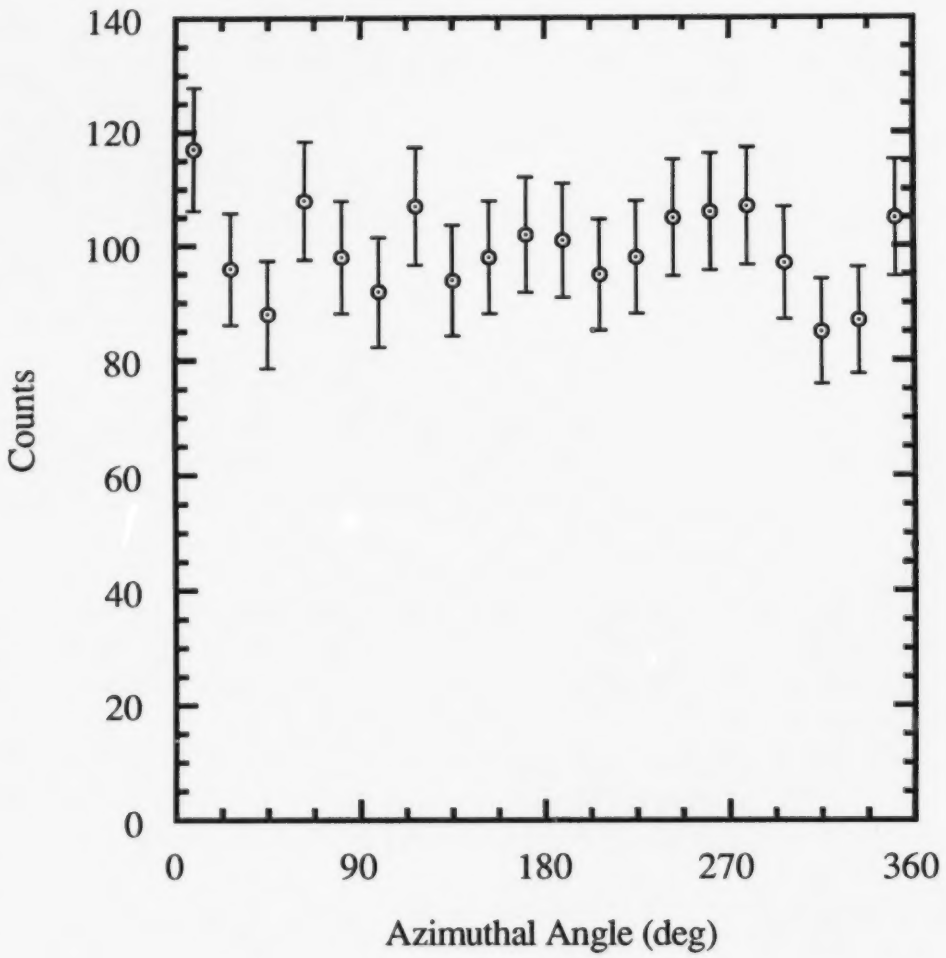

Figure 4.9 Distribution of the azimuthal angle for three track $pp\pi^-$ events.

$$\frac{dE}{dx} = D\left(\frac{z}{\beta}\right)^2 \left[\ln(A\beta^2\gamma^2) - \beta^2\right] , \qquad (4.4)$$

where D and A are constants that depend on the material type, and z is the charge of the incident particle. The energy loss depends on the particle's velocity through β and γ, where

$$\beta = v/c \qquad (4.5)$$

and

$$\gamma = (1 - \beta^2)^{-1/2} . \qquad (4.6)$$

Figure 4.10 shows the energy loss obtained from the Bethe-Bloch formula as a function of kinetic energy. Protons and pions have distinct curves on such a plot particularly in the low energy region. This may be exploited for particle identification purposes. Figure 4.11 is a $\Delta E/\Delta x$ vs. E plot obtained from SALAD for $pp\pi^-$ events. The lines of figure 4.10 are smeared out due to the resolution of SALAD. However, two clusters of particles may be identified. The first cluster, with the lowest ΔE and E values, is due to pions and the second cluster is due to protons. This stopping power histogram was linearized to obtain figure 4.12. Two peaks corresponding to pions and protons, respectively, may be clearly identified on this plot.

No particle identification cuts were applied in this analysis since many of the particles of interest stop in the wire chambers or in the ΔE scintillators. Moreover, the strong absorption of the π^- in the scintillators obscures any determination of the π^- kinetic energy. As evident by the well defined loci in figure 4.11, however, the stopping power determinations are still well defined.

The combined effect of low particle energies and relatively high detector thresholds results in drastically reducing the number of detected $pp\pi^-$ events. The highest photon energy was ~290 MeV. Since a pion is formed, 140 MeV are lost in such a process. The remaining 150 MeV are distributed as kinetic energy among the three outgoing particles. In this energy region, the quasi-free process is dominant and one of the protons is a spectator which does not share this energy. This proton will likely lose its energy in the walls of the detector and not make it all the way to the ΔE

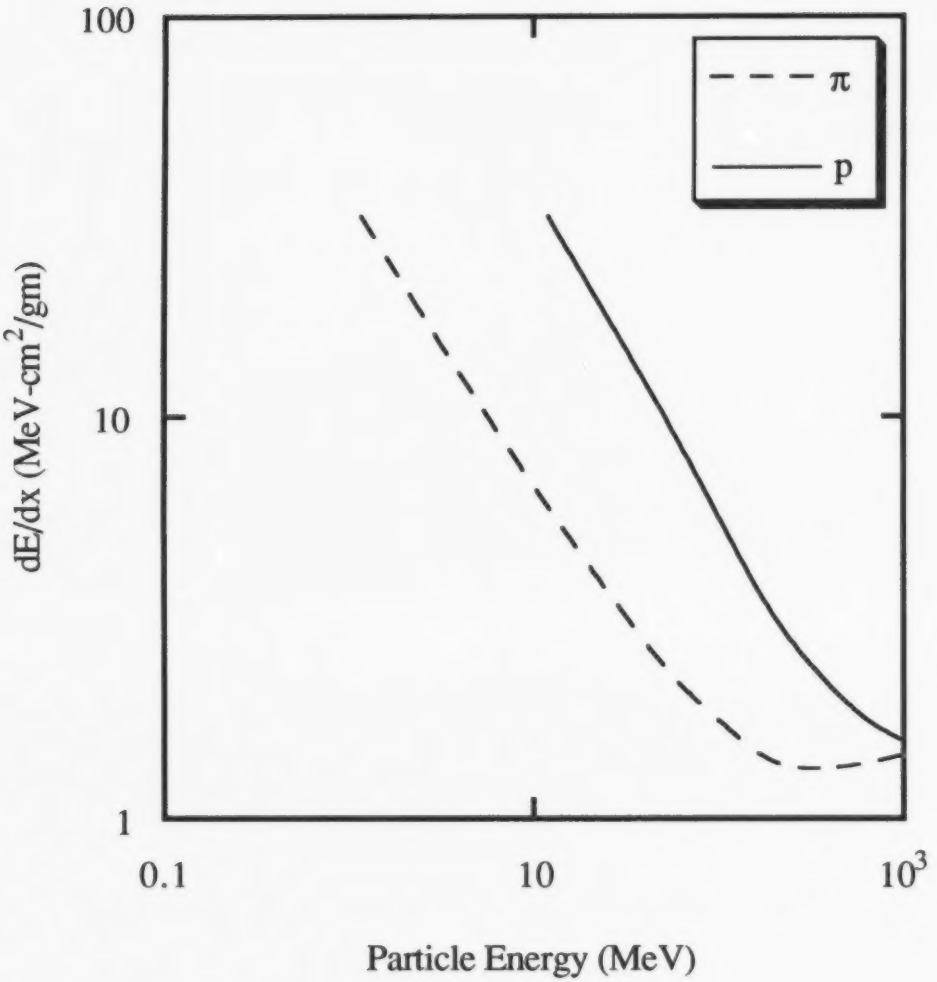

Figure 4.10 Stopping power as a function of energy for protons and pions as calculated from the Bethe-Bloch formula obtained from ref. 18.

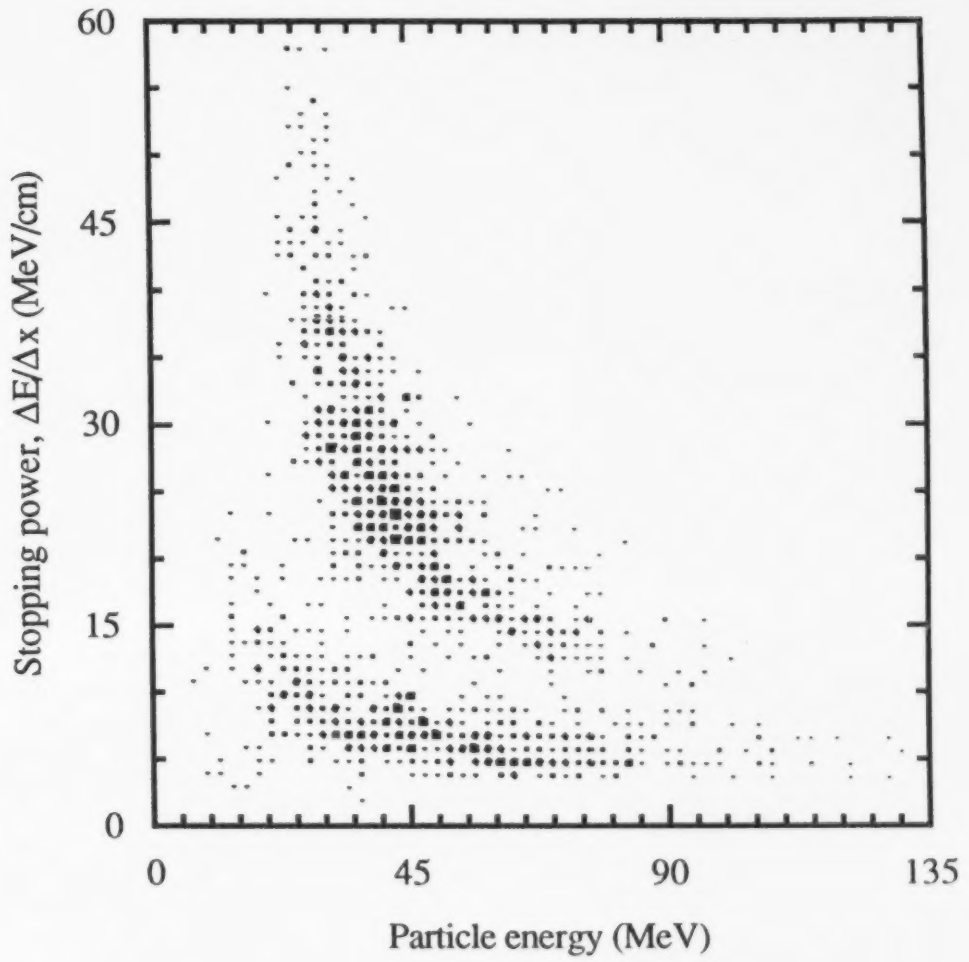

Figure 4.11 Stopping power vs. energy for three track $pp\pi^-$ events.

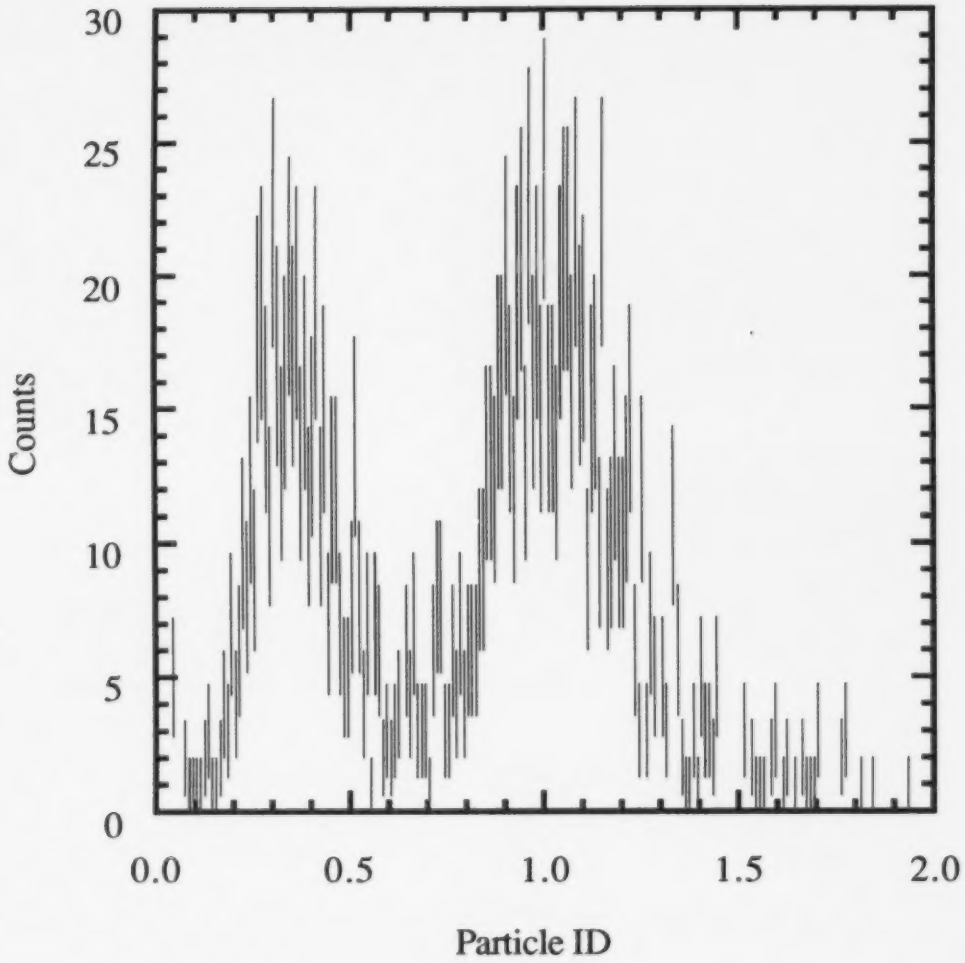

Figure 4.12 Linearized stopping power histogram for three track $pp\pi^-$ events. The peak near 0.35 corresponds to the stopping power of pions, while that near 1.0 corresponds to that of protons.

scintillators. If such a proton successfully passes through the inner and at least one of the outer wire chambers, a track may result. As seen in section (4A) from table 4.1, most events are not of this type. It is worth mentioning at this point that the requirement of the presence of three tracks in the analysis demands that the spectator nucleon momentum be relatively large, and thus discriminates against the quasi-free process.

C. Event Selection

Since pion kinetic energies may not be used and beam energies are low, two decisions were made. At the hardware level, the usual trigger requirement that a tagger signal be present was dropped when three SALAD telescope signals were present, as discussed in section 2D. At the software level, only three track events were analyzed to allow for a high confidence level in the analyzed events. At present, extensive background tests have not been completed, and it is not clear whether it will be possible to analyze two track events. As previously shown, if two track events may be analyzed with confidence, the number of $pp\pi^-$ events obtained will increase substantially.

In this experiment, an analytic solution for the three body final state kinematics drastically reduces the number of $pp\pi^-$ events. Most of the two track events are expected to result from a proton and a pion since the quasi-free process is dominant in this energy range. If the event is untagged, the available quantities are not enough to fully determine the three-body final state kinematics (since the pion kinetic energy is not reliably determined). If the event is tagged, the kinematic equations may be solved only if both the ΔE and E values were measured for both particles, otherwise two solutions result from the two possible track permutations with no way to identify the correct one. Three track events are predominantly untagged. The resulting six angles may be used to solve for the photon energy. The resulting equation is quadratic. Two solutions therefore result. For three track events, three possible permutations exist for the particle identifications resulting in a total of six solutions for the photon energy per event. To make matters worse, solutions for the photon energy in terms of the six angles are sensitive to small variations in these angles and, hence, the angular resolution of SALAD does not allow for an analytic solution.

A fitting program was therefore used. The inputs to this program are all the measured quantities: the six θ and ϕ angles, as well as the ΔE, E, and E_γ energies if they have been measured. If the event is untagged, a starting value is assigned to E_γ. The angles and the photon energy are used to solve the kinematic equations. Once the vertex energies are determined, the energies deposited in the ΔE and E scintillators may be calculated by tracing the particle's path through the detector. A χ^2 value that takes into account all the observables and their respective weights may then be calculated. The χ^2 is minimized by varying the angles and the photon energy around their measured values within the range of their errors. If the event is untagged, a search is performed over the possible range of the photon energy.

Three possible permutations exist for the track identifications (any one of the three tracks may be a π^-). The above steps are therefore repeated for each possible permutation, and the one with the smallest χ^2 is chosen as the correct permutation. If the pion stops in the ΔE (E) scintillator, the contribution of the ΔE (E) to the χ^2 value is given zero weight. Moreover, if two tracks point to the same scintillator it is not possible to measure their individual energies. Such events are immediately rejected and no attempt is made for a χ^2 minimization.

The χ^2 distribution is shown in figure 4.13. A kinematic cut was applied such that only events with a $\chi^2 < 2.5$ are considered. The distribution is wider than expected apparently because the resolution of the calorimeter has been underestimated. Figure 4.12 shows the particle identification plot for events that satisfy this χ^2 cut. The two peaks corresponding to pions and protons may be readily identified on this plot. As mentioned in section 4A no particle identification cuts were imposed in the analysis. Extensive background tests are yet to be completed. No estimate currently exists for the number of lost $pp\pi^-$ events or possible background contaminations.

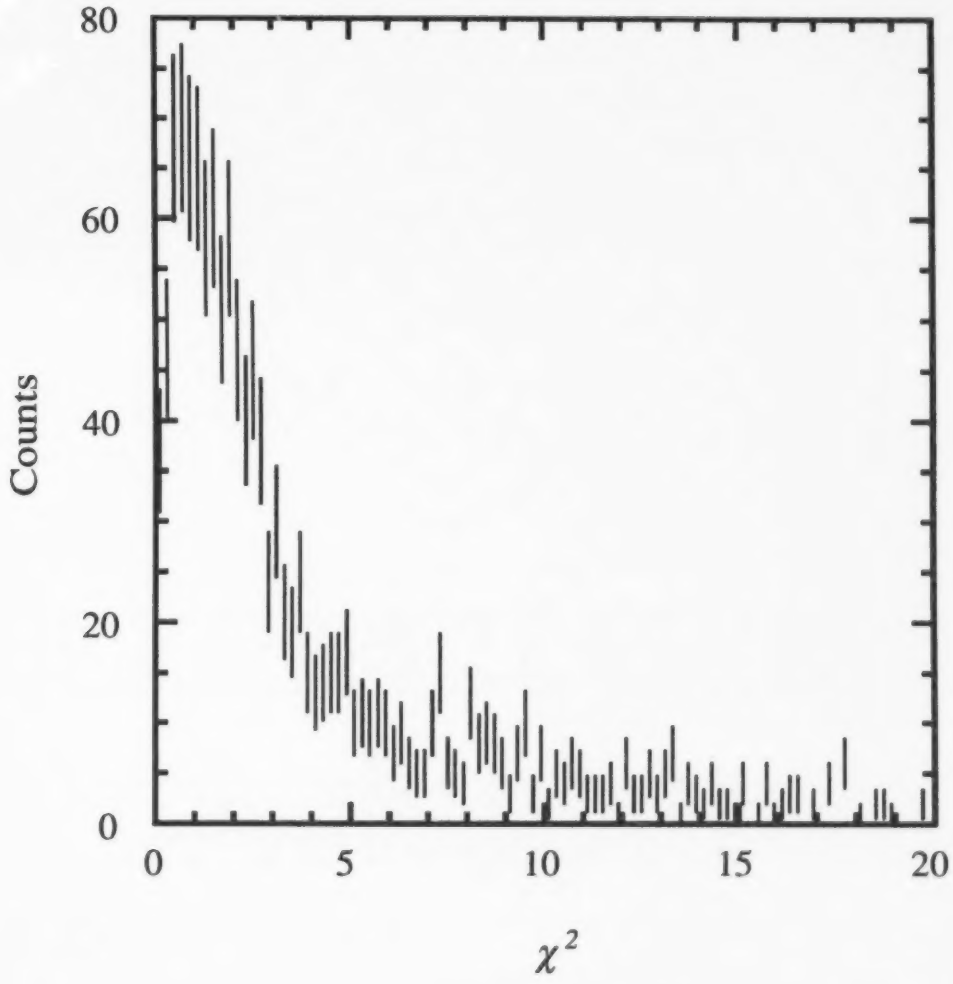

Figure 4.13 Kinematic χ^2 distribution for three track $\gamma D \rightarrow pp\pi^-$ events.

D. Monte Carlo Simulations

For two body final states, the number of particles $N(\theta)$ observed by SALAD at a given angle θ may be written as

$$N(\theta) = N_I N_T \frac{d\sigma}{d\Omega} d\Omega_{eff}(\theta) , \tag{4.7}$$

where N_I is the number of incident particles, N_T is the number of target nuclei per unit area, $d\sigma/d\Omega$ is the reaction cross section, and $d\Omega_{eff}(\theta)$ is the effective solid angle given by

$$d\Omega_{eff}(\theta) = \varepsilon(\theta)\, 2\pi \sin\theta\, d\theta , \tag{4.8}$$

where $\varepsilon(\theta)$ is the efficiency of SALAD. If this efficiency is known the reaction cross section may be obtained

$$\frac{d\sigma}{d\Omega}(\theta) = \frac{N(\theta)}{2\pi N_T N_I \sin\theta\, \varepsilon(\theta)\, d\theta} . \tag{4.9}$$

The efficiency may be calculated from Monte Carlo simulations. Two important factors may contribute to this efficiency. First, the total solid angle subtended by SALAD is slightly less than 4π. Particles originating from a certain point inside the target with certain trajectories may pass through SALAD undetected. Second, since outgoing particles loose energy as they traverse the detector, only those with enough energy to reach the calorimeter and deposit a sufficient amount of energy that exceeds the threshold requirement will cause a trigger. All of these effects are considered in the Monte Carlo. The shape and size of the beam are also included. The energy lost in the walls of the detector is calculated from the known vertex energy and trajectory of that particle, and a determination is made as to whether this particle will cause a trigger. The efficiency $\varepsilon(\theta)$ is thus defined as the fraction of the total number of generated events that are expected to be detected.

In order to test the efficiency calculation, a calibration measurement of the counting rates and angular distributions for p-p elastic scattering were measured with SALAD at TRIUMF in October, 1988, at 220 MeV incident energy[14]. The resulting angular distribution was compared to the results of previous experiments. As may be

seen in figure 4.14 the agreement is reasonable and yields confidence in the calculated efficiency.

The cross section for a three body final state reaction may be written as[19]

$$d^9\sigma = \frac{1}{N_i} \sum_i \sum_f \frac{d^3\mathbf{p}_1'}{2E_1'} \frac{d^3\mathbf{p}_2'}{2E_2'} \frac{d^3\mathbf{p}_3'}{2E_3'} \delta^3(\mathbf{p} - \mathbf{p}') \, \delta(E - E') \, |T_{fi}|^2 \qquad (4.10)$$

where the initial state kinematics are defined by

$$E = E_1 + E_2 , \qquad \mathbf{p} = \mathbf{p}_1 + \mathbf{p}_2 \qquad (4.11)$$

and the final state kinematics are defined by

$$E' = E_1' + E_2' + E_3' , \qquad \mathbf{p}' = \mathbf{p}_1' + \mathbf{p}_2' + \mathbf{p}_3' \qquad (4.12)$$

$$T_{fi} = \langle f | T | i \rangle \qquad (4.13)$$

where

$$T = V + \frac{1}{E - H_0} T \qquad (4.14)$$

which includes all the dynamics. The rest of equation 4.10 is the kinematic three body phase space factor.

The Monte Carlo includes this three body final state phase space factor, as well as the efficiency of SALAD. Monte Carlo events may be generated assuming tagged or untagged events. Since both types of events are considered in this analysis, a combination of tagged and untagged events was used depending on the energy of the incident photon. If the incident photon energy is above the tagger energy range, the event is considered untagged, and a bremsstrahlung photon energy distribution is assumed.

Other factors should be considered in the Monte Carlo and will be the subject of future work. Energy losses due to nuclear interactions may contribute to the energy loss. Wire efficiencies, particularly in the bad region of wire chamber 3 should be considered. The measured pedestals have a finite width which should be accounted for. Light outputs, resolutions, and scintillator thresholds should also be further investigated.

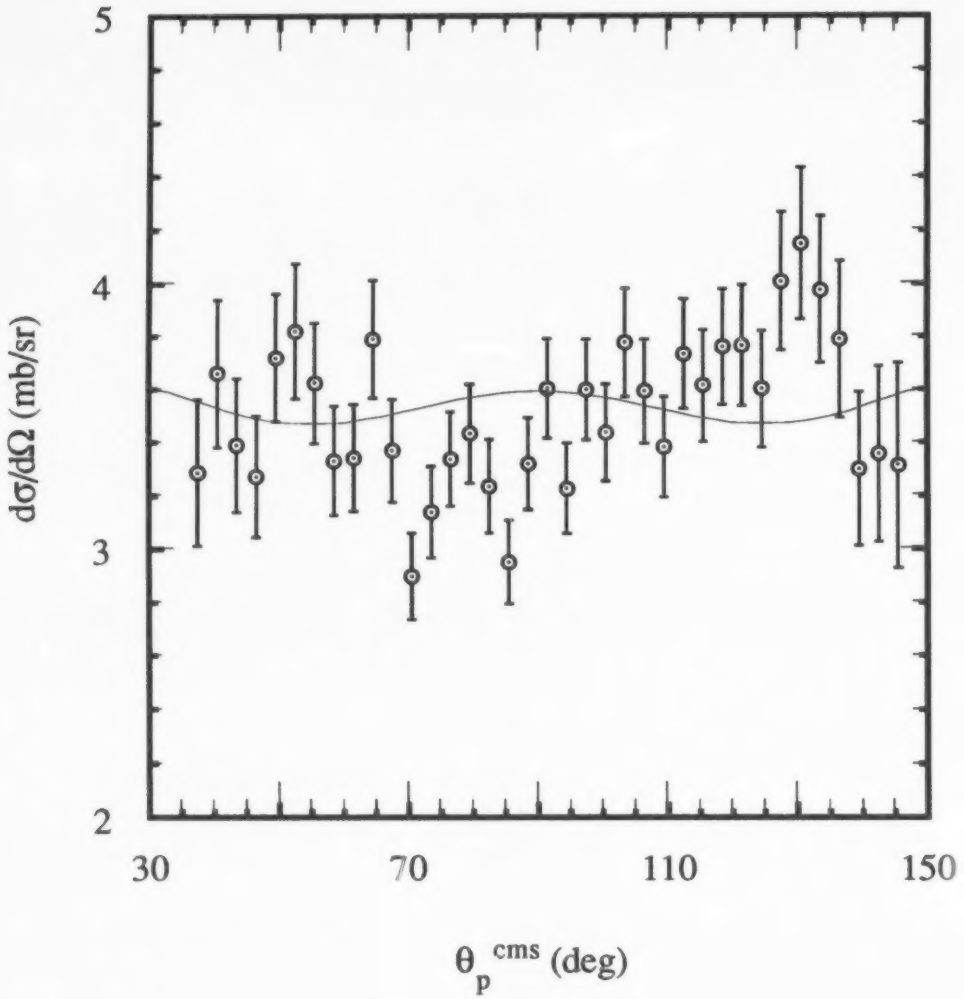

Figure 4.14 p-p elastic scattering cross section at $E\gamma$= 220 MeV as measured by SALAD.

The generated Monte Carlo events are stored on disk. These events are analyzed with the same analysis code used to analyze real data, and the same cuts are therefore applied. This ensures that any observed deviations of real data from the expected Monte Carlo distributions, apart from the few refinements that should be made in the Monte Carlo, are indeed due to dynamical physical effects.

Dynamics may also be included in the Monte Carlo. In this analysis comparisons are made between our data and the calculations described in the previous chapter for various ingredients of the transition matrix. The Monte Carlo allows for a large number of variables to be histogrammed and compared to the data. Results and conclusions that may be learned from these comparisons are presented and discussed in the next chapter.

Chapter 5

Results and Discussion

In the region of the Δ resonance, the $\gamma D \rightarrow pp\pi^-$ reaction may occur in two steps. In the first step, the deuteron disintegrates into a proton and a Δ

$$\gamma D \rightarrow p\Delta^{\circ}. \tag{5.1}$$

For the two body disintegration, the three particles (photon, proton and Δ) should lie in one plane so as to conserve momentum. The outgoing Δ is unstable (mean life, $\tau = 10^{-24}$ seconds) and decays into a proton and a pion

$$\Delta^{\circ} \rightarrow p\pi^-. \tag{5.2}$$

To conserve momentum, the Δ, the decay proton, and the pion lie in one plane. The resulting two planes and some variable definitions are shown in figure 5.1 In a coordinate system for which the z-axis is defined by the direction of the Δ, the angle between the two planes is the azimuthal angle of the pion. The two angles ϕ_π and θ_π are defined in this coordinate system, whereas the Δ scattering angle, θ_Δ, is defined in a coordinate system for which the direction of the photon defines the z-axis. The scattering angles of the pion, ϕ_π and θ_π, may then be boosted to the Δ rest frame, and the scattering angle of the Δ, θ_Δ, may be boosted to the γ-D center of mass frame.

The resulting distributions of the data in terms of θ_Δ^*, θ_π^* and ϕ_π^*, together with the microscopic calculations are shown in figure 5.2. The efficiency of SALAD is folded with the theoretical calculations. Differential cross sections in the five variables θ_Δ^*, θ_π^*, ϕ_π^*, E_γ and Q_Δ were calculated. The differential yield is given by

$$Y_5(\theta^*_\Delta,\theta^*_\pi,\phi^*_\pi,E_\gamma,Q_\Delta) = \frac{d^5\sigma}{d\theta^*_\Delta\, d\Omega^*_\pi\, dE_\gamma\, dQ_\Delta}(\theta^*_\Delta,\theta^*_\pi,\phi^*_\pi,E_\gamma,Q_\Delta) \times$$

$$\varepsilon(\theta^*_\Delta,\theta^*_\pi,\phi^*_\pi,E_\gamma,Q_\Delta)\, N_\tau\, N_\gamma(E_\gamma) \qquad (5.3)$$

where N_τ is the number of target nuclei and N_γ is the number of particles in the incident beam. The yield as a function of any of these variables may be calculated by integrating over the other four. For the variable ϕ_π^* we have

$$Y(\phi^*_\pi) = \int\int\int\int d\theta^*_\Delta\, d\theta^*_\pi\, dE_\gamma\, dQ_\Delta\, Y_5(\theta^*_\Delta,\theta^*_\pi,\phi^*_\pi,E_\gamma,Q_\Delta) \qquad (5.4)$$

The cross sections and efficiencies were calculated for ten bins in each variable, resulting in a total of 10^5 bins. At present, the normalizations of the data have not been determined so the normalizations of the theoretical curves are arbitrary. A bremsstrahlung distribution is considered to account for the dependence of N_γ on the photon energy. The error bars are statistical. Estimates of the systematic errors are yet to be completed. The microscopic calculations shown are described in detail in the third chapter.

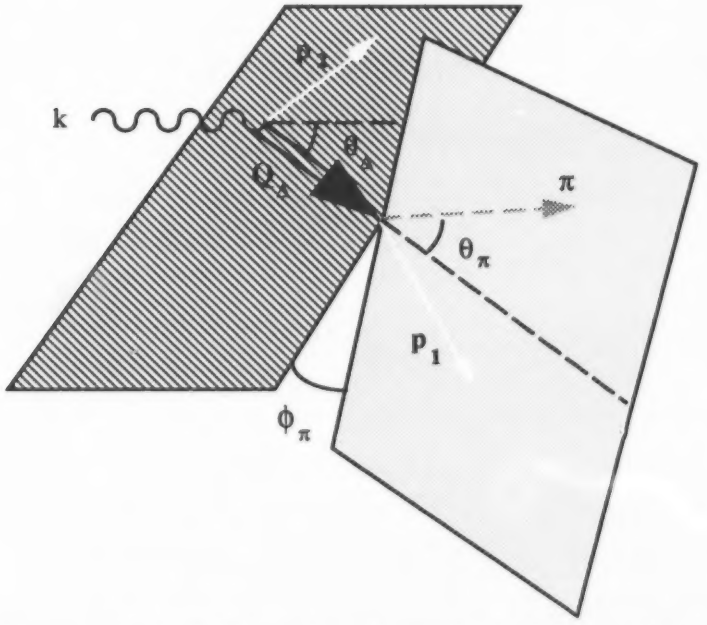

Figure 5.1 Definitions of the kinematic variables used to describe the $\gamma D \rightarrow pp\pi^-$ reaction.

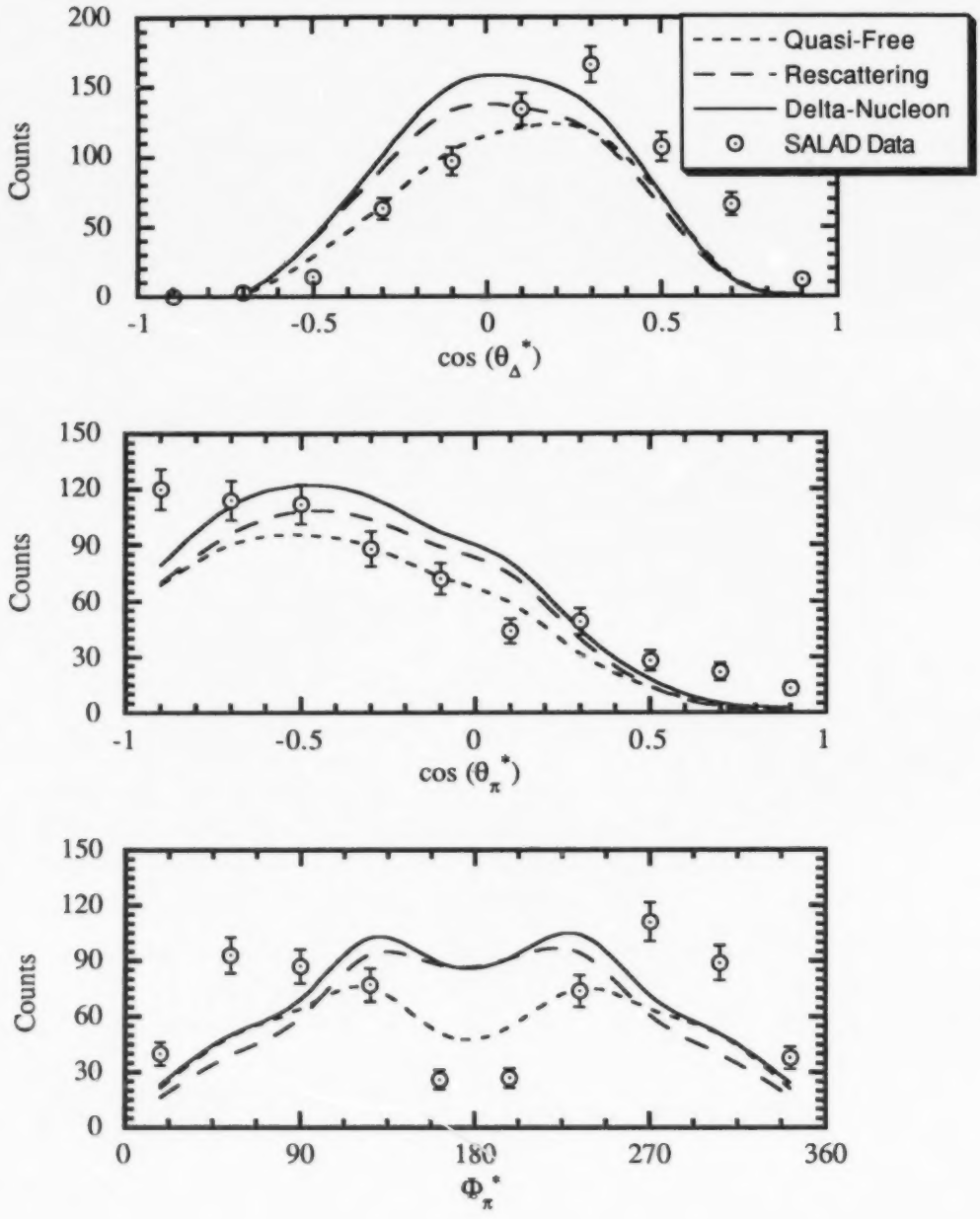

Figure 5.2 Distributions of $\cos(\theta_\Delta^*)$, $\cos(\theta_\pi^*)$, and Φ_π^* for three track $pp\pi^-$ events. The data are from the SALAD run of June 1992. The theoretical curves are calculated by J. M. Laget.

To obtain the dotted curve, only the quasi-free diagram (figure 3.5 diagram I) was included in the calculation. The dashed curve includes the quasi-free diagram, the one-loop π-N and N-N rescattering diagrams (figure 3.5 diagrams II and III), and the two-loop π-N followed by N-N rescattering diagram (figure 3.5 diagram IV). Another calculation has also been made for the quasi-free amplitude with rescattering corrections but excluding the double loop diagram. The difference between the two calculations is negligible. It should be remembered at this point that the Δ-N interaction calculation is only exploratory. The phase shifts used to parametrize the Δ-N interaction were obtained by Ferreira and Dosch[21] and have not been adjusted to improve agreement between the calculations and the data. Moreover, other diagrams that might involve a Δ-N interaction have not been included in the calculation, in particular those of figure 5.3 for which the π-N and N-N rescattering is preceded by the Δ-N interaction. The inclusion of the contributions of these diagrams in the Δ-N interaction calculations will also be the subject of future work. As for the experimental points, normalizations and error estimates are necessary before a statement is made concerning the size of these deviations.

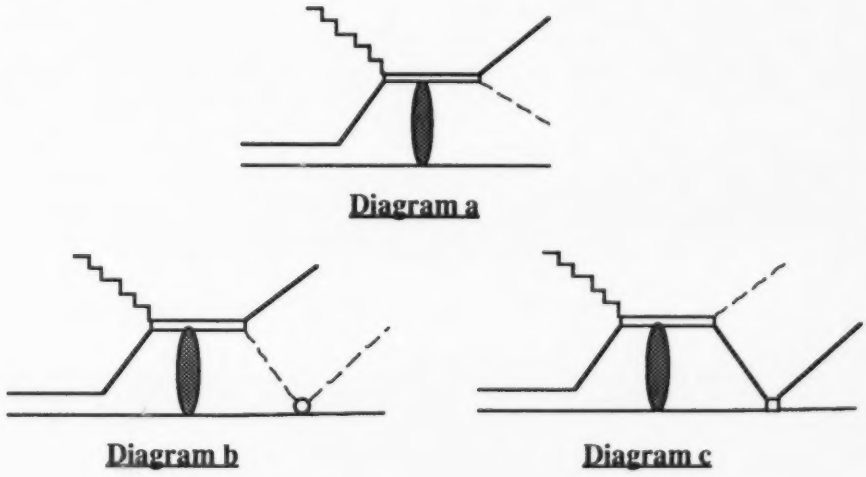

Figure 5.3 Feynman diagrams for the Δ-N interaction.

Due to the limited statistical accuracy in this experiment, detailed explorations of particular regions of phase space are not practical. We have, therefore, limited this present analysis to the investigation of the behavior of these interactions in different regions of the pπ mass, Q_Δ. Figure 5.4 shows the same plots of figure 5.2 except that the pπ mass is restricted to values below 1110 MeV. The calculation shows a strong deviation between the curve which includes the Δ-N interaction and the other two curves. Although the Δ-N interaction is expected to be small away from the peak of the Δ resonance, interference effects between the different amplitudes may result in strong deviations. Moreover, when the pπ mass is restricted to small values, to conserve energy, the other proton must carry a relatively large momentum, a signal of strong final state interactions. As may be seen from this figure, the size of the difference between these curves is bigger than the size of the error bars, and hence, once the data are normalized, it should be possible to make a statement concerning the Δ-N interaction calculation. In figures 5.5 and 5.6 the pπ mass is restricted to the regions 1110-1140 MeV and >1140 MeV, respectively. Only small deviations between the quasi-free calculation and those which include rescattering effects and Δ-N interactions are seen in this pπ mass range, particularly in figure 5.5. Events plotted in figure 5.6, for which the pπ mass is restricted to high values, correspond to photon energies near the tail of bremsstrahlung distribution, and are more sensitive to the exact shape of this distribution.

The analysis presented here is for only ~50% of the existing data from the $\gamma D \rightarrow pp\pi^-$ run of June 92. Analysis of the complete set of data is yet to be completed. The remaining data include a set of runs with multiplicity 2 forced trigger (section 2D). These events should be analyzed separately since the efficiency of the SALAD detector is different due to the different trigger requirement. Moreover, this analysis is only preliminary. Several refinements, modifications and tests are still to be made.

As previously mentioned, the wire chamber parameters (of eqn. 2.3) were determined from the analysis of one of the wire chamber calibration runs. Several other runs exist and will be analyzed. The parameters will then be determined by summing up the data from all the runs. Similarly, only one cosmic run was used to determine the gains of the ΔE and E scintillators. The other existing runs will be analyzed and summed to determine the average gain calibrations.

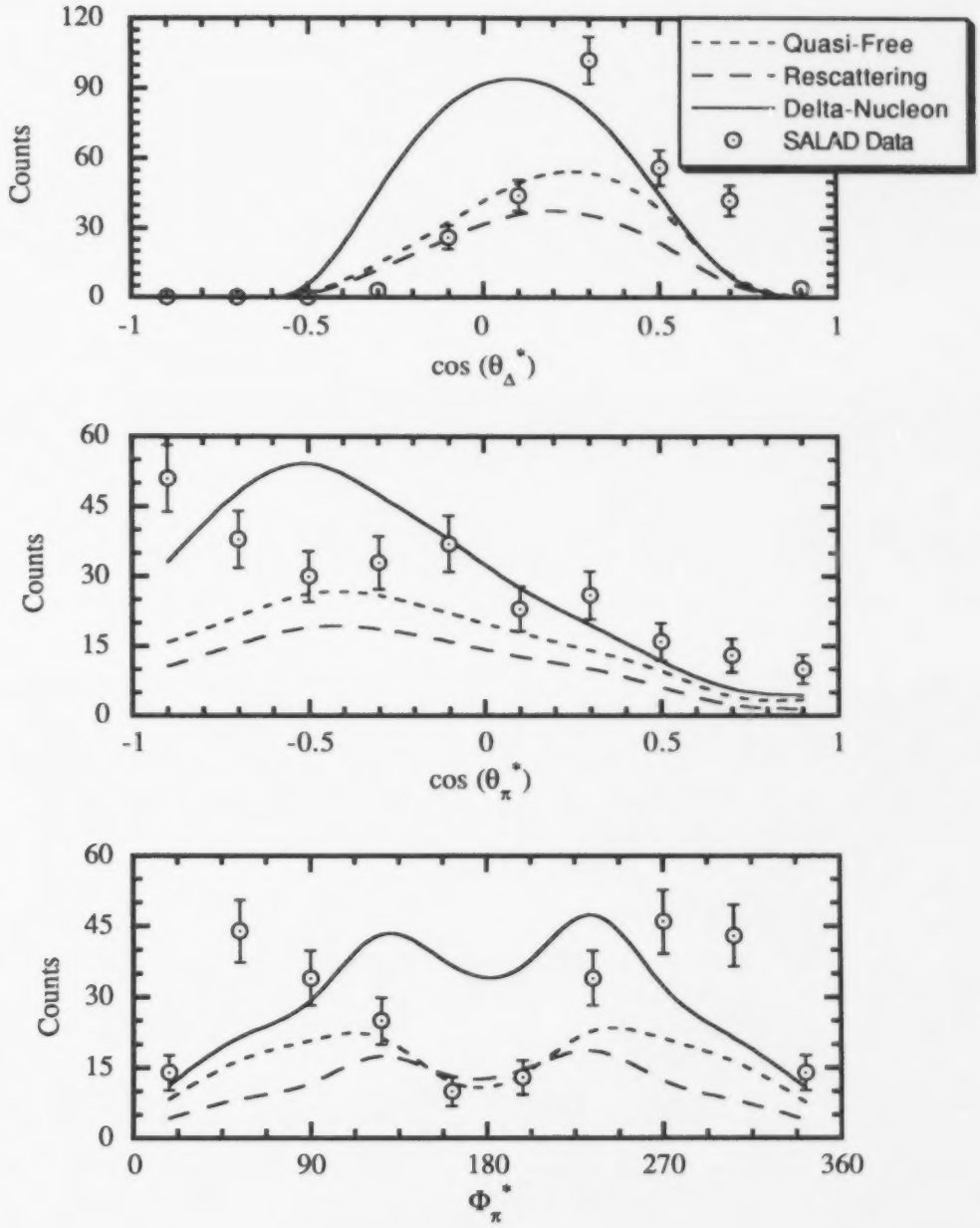

Figure 5.4 Distributions of $\cos(\theta_\Delta^*)$, $\cos(\theta_\pi^*)$, and Φ_π^* for three track $pp\pi^-$ events. The $p\pi$ mass is restricted to values below 1110 MeV. The data are from the SALAD run of June 1992. The theoretical curves are calculated by J. M. Laget.

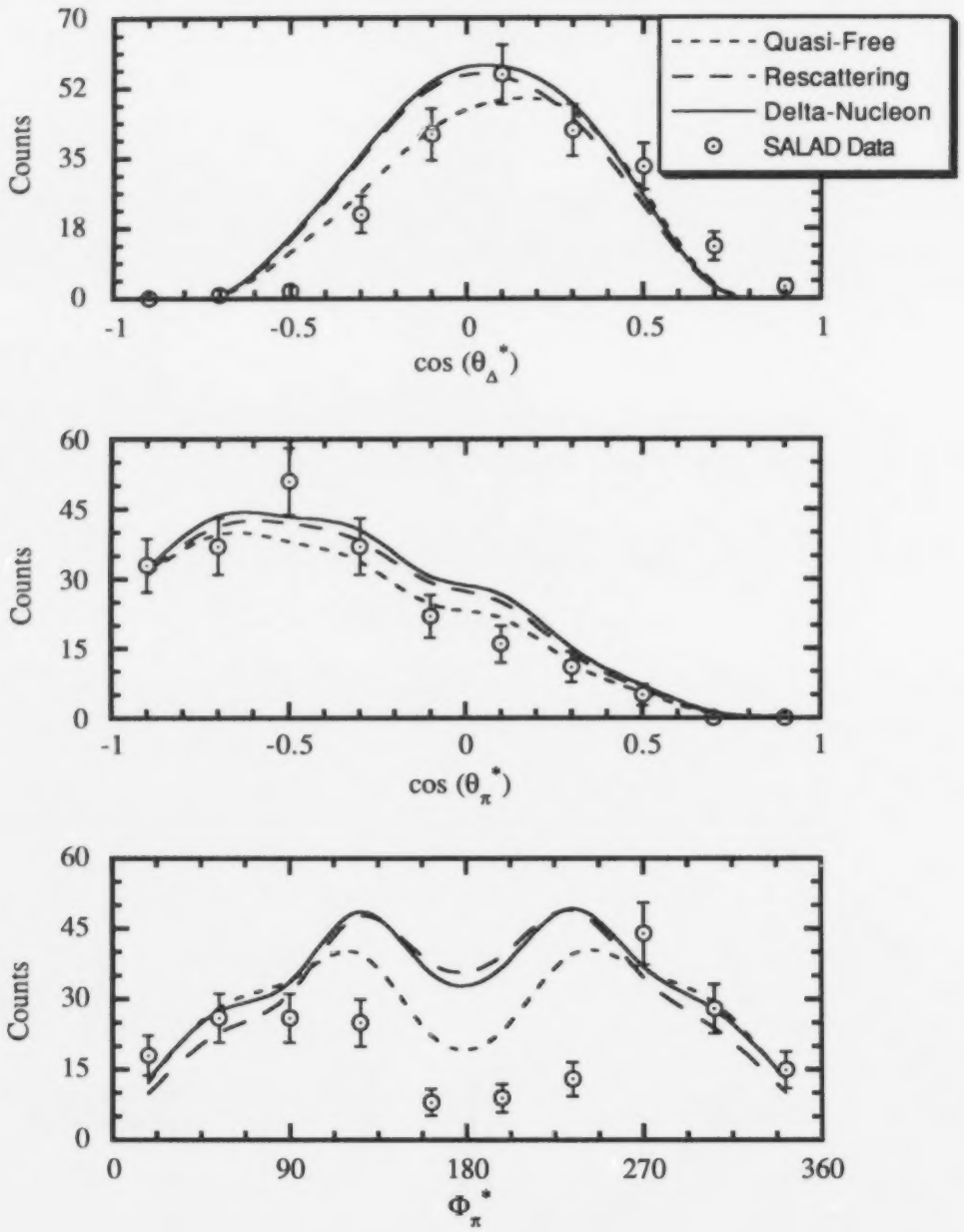

Figure 5.5 Distributions of $\cos(\theta_\Delta^*)$, $\cos(\theta_\pi^*)$, and Φ_π^* for three track $pp\pi^-$ events. The $p\pi$ mass is restricted to values between 1110 MeV and 1140 MeV. The data are from the SALAD run of June 1992. The theoretical curves are calculated by J. M. Laget.

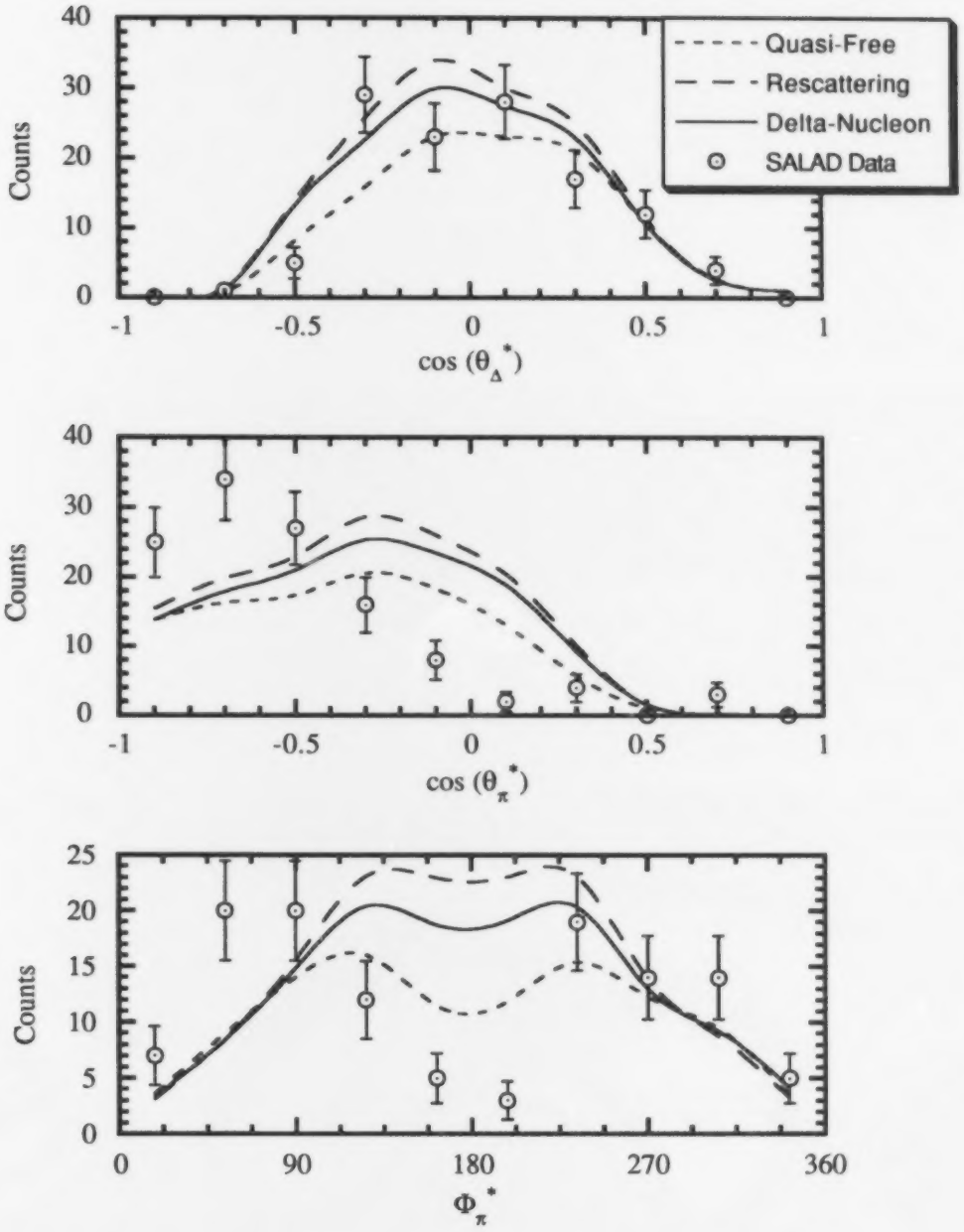

Figure 5.6 Distributions of $\cos(\theta_\Delta^*)$, $\cos(\theta_\pi^*)$, and Φ_π^* for three track $pp\pi^-$ events. The $p\pi$ mass is restricted to values above 1140 MeV. The data are from the SALAD run of June 1992. The theoretical curves are calculated by J. M. Laget.

Extensive background tests of the fitting program will also be made. The width of the χ^2 distribution will be further investigated. This involves a further investigation of the resolution in the measured quantities (ϕ, θ, ΔE , E and E_γ) used as inputs to the fitting program. Uncertainty currently exists in the resolutions of the ΔE and E scintillators for this data set. Preliminary analysis has indicated some sensitivity in the χ^2 distribution width to these resolutions. The fitted data will be further tested for background contaminations. Two track events will be analyzed separately and background tests will be made to determine whether $pp\pi^-$ events may be extracted with a good confidence level.Normalization of the data involves the determination of the total number of photons in the incident beam. For tagged events the number of photons coming out of the radiator will be determined from the focal plane scalars. To determine the actual number of photons in the incident beam (i.e. that make it into the target region) tagging efficiency measurements will be analyzed (section 2A). For untagged events, a bremsstrahlung distribution will be used. Further investigation of the shape of this distribution will be made.

Several refinements should also be made in the Monte Carlo. These include the shape of the bremsstrahlung distribution described above, allowing nuclear interactions in the scintillators, and allowing for a finite pedestal width. On the theoretical side, as mentioned above, diagrams b and c of figure 5.3 should be included in the calculation of the $\gamma D \rightarrow pp\pi^-$ cross section. These calculations will be made by J. M. Laget.

References

(1) V. Rossi et al., Nuovo Cimento **13A** (1973) 59.

(2) P. E. Scheffler and P. L. Walden, Phys. Rev. Lett. **24** (1970) 952.

(3) P. Benz et al., Nuc. Phys **B65** (1973) 158.

(4) P. E. Argan et al., Nuc. Phys. **A296** (1978) 373.

(5) J. M. Laget, Nuc. Phys. **A296** (1978) 388.

(6) P. E. Argan et al., Phys. Rev. Lett. **41** (1978) 86.

(7) J. M. Laget, Nuc. Phys. **A335** (1980) 267.

(8) J. M. Laget, Phys. Rep. **69** (1981) 1.

(9) Stanley Kowalski, Proc. of the 1989 IEEE Part. Acc. Conf., **1** (1989).

(10) L. O. Dallin, Proc. of the 1989 IEEE Part. Acc. Conf., **1** (1989).

(11) J. L. Laclare and R. Servanckx, IEEE Trans. Nucl. Sci. NS-18 (1971) 207.

(12) R. Servanckx and J. L. Laclare, IEEE Trans. Nucl. Sci. NS-18 (1971) 204.

(13) E. B. Cairns et al., Nucl. Instr. and Meth. **A321** (1992) 109.

(14) P. P. Langill, M.Sc. Thesis, University of Alberta (1989).

(15) J. M. Laget, Nuc. Phys. **A312** (1978) 265.

(16) J. M. Laget, Can. J. Phys. **62** (1984) 1046.

(17) I. Blomqvist and J. M. Laget, Nuc. Phys. **A280** (1977) 405.

(18) W. R. Leo, Techniques for Nuclear and Particle Physics Experiments, Springer-Verlag (1987).

(19) M. Nikolic', Kinematics and Multiparticle Systems, Gordon and Breach Science Publishers Inc. (1968).

(20) J. J. Sakurai, Modern Quantum Mechanics, Addison Wesley Publishing Company (1985).

(21) E. Ferreira and H. G. Dosch, Phys. Rev. **C42**, 2334 (1990).